6-2011

Fabry-Perot Observations of Midlatitude Neutral Winds and Atmospheric Gravity Wave Activity

Marjory Anne Katon
Embry-Riddle Aeronautical University - Daytona Beach

FABRY–PEROT OBSERVATIONS OF MIDLATITUDE NEUTRAL WINDS AND ATMOSPHERIC GRAVITY WAVE ACTIVITY

By

Marjory Anne Katon

A Thesis Submitted to the

Physical Sciences Department

In Partial Fulfillment of the Requirements for the Degree of

Master of Science in Engineering Physics

Embry-Riddle Aeronautical University

Daytona Beach, Florida

June 2011

FABRY–PEROT OBSERVATIONS OF MIDLATITUDE NEUTRAL WINDS AND ATMOSPHERIC GRAVITY WAVE ACTIVITY

by

Marjory Anne Katon

This thesis was prepared under the direction of the candidate's thesis committee chair, Dr. John M. Hughes, Department of Physical Sciences, and has been approved by the members of the thesis committee. It was submitted to the Department of Physical Sciences and was accepted in partial fulfillment of the requirements of the Degree of

Master of Science in Engineering Physics

THESIS COMMITTEE:

Dr. John M. Hughes, Chair

Dr. Gulamabas Sivjee, Member

Dr. Alan Liu, Member

Dr. Peter Erdman
MSEP Graduate Program Coordinator

Dr. Michael Hickey
Department Chair, Physical Sciences

Dr. Robert Oxley
Associate Vice President for Academics

30 June 2011
Date

ABSTRACT

Author:	Marjory Anne Katon
Title:	Fabry–Perot Observations of Midlatitude Neutral Winds and Atmospheric Gravity Wave Activity
Institution:	Embry-Riddle Aeronautical University
Degree:	Master of Science in Engineering Physics
Year:	2011

The mesosphere and lower thermosphere displays a wide range of dynamical phenomena resulting in a complex and variable region. Governed primarily by fluid dynamics, the motion of the upper atmosphere is modulated by a number of atmospheric waves propagating upward from various sources in the lower atmosphere. Among these are atmospheric gravity waves which have been recognized as a major source of momentum and energy in the mesosphere and lower thermosphere as well as a major factor in the dynamic coupling between the troposphere and lower thermosphere. A Fabry–Perot interferometer possessed by the Space Physics Research Laboratory at the Embry–Riddle Aeronautical University, Daytona Beach, FL campus was used to measure Doppler shifts in the atomic oxygen green line emission which originates from an altitude of 96 km. The process of extracting the horizontal winds from the detected Doppler shifts and the resulting time series of the zonal and meridional winds at that altitude is presented. The winds at various nights as well as the average winds for two months were compared with the Horizontal Wind Model 07. Fourier analysis was performed on the time series to determine intrinsic periodicities of the calculated winds. The spectral power of three different nights,

each with different weather to the west of Daytona Beach is also presented. Each spectrum depicted the shorter period harmonics of the semi–diurnal tide. Gravity wave activity was correlated to a thunderstorm on the west coast of Florida for one night. The peak of the recorded gravity wave had an observed frequency of 1.663 hr^{-1} and a intrinsic frequency of 0.0622 hr^{-1}. The wave's direction of propagation was in agreement with the direction of the observed winds at the time of the wave's peak.

ACKNOWLEDGEMENTS

First and foremost I would like to thank my thesis advisor Dr. Hughes for making this body of work possible. Thank you for your guidance and direction throughout this process as well as your patience with me during the writing process. I am truly grateful to have been able to work with you and appreciate all the advice you have given me this past year.

To my committee members, Dr. Sivjee and Dr. Liu thank you for taking the time to serve on my committee. Your knowledge and expertise on the subject matter is remarkable and I am very glad I was able to work with you both.

Thanks must be given to those at SPRL. Adam Tishman, thank you for teaching me all that you know about the Fabry–Perot and for your continuous support. Charles Mutiso, thank you for your unconditional help especially during the writing process. And Zach Tejral, thank you for your company at the lab and being on–call for times I've needed an extra set of hands.

To all of my classmates (Lex, Vince, Christina, Steve, Taka, Chris, Tom, Alex and Sathish) thank you for all your support and the fun times in the TA office and in class. To my friends outside of the Lehman building (Tom, Amanda, Betty, Audrey, Kavita, Joelle, Caitlin, Michael, JP, Maria, Nikki, Suzi and Shane), your constant support has been amazing throughout this process, thank you.

Finally, thank you to my family. Mom and Dad, thank you for your selflessness in raising me and supporting me in everything I have taken on. I am indebted to all that you have given me throughout the years and to the experiences you have made possible. To my brother, Matthew, thank you for listening to me when I would call and always being there for me.

To all my friends, family and professors unmentioned, thank you for everything.

Marjory Katon

June 2011

Contents

List of Figures

Chapter 1

Background

1.1 Neutral Atmosphere

Earth's neutral atmosphere extends from the surface to about 100,000 km where it meets interplanetary space [Prolss, 2004]. About 99.9997% of the neutral atmosphere, however, lies below 100 km. At ground level, the atmosphere is composed of 78.1% molecular Nitrogen (N_2), 20.9% molecular Oxygen (O_2), 0.93% Argon (Ar), and various trace elements such as Carbon Dioxide (CO_2), Neon (Ne), Helium (He) make up the remaining 0.07% [Hughes, 2008]. Among the most important properties of the atmosphere are its pressure, density, temperature and composition, all of which are dependent on each other. These properties as well as physically important processes give way to different classifications and nomenclatures of the atmosphere, the most common being the vertical temperature profile.

The most basic physical feature of the atmosphere is the decrease of pressure and density with increasing altitude. This feature can be shown through the hydrostatic equation which is derived by considering a massless membrane of some area where

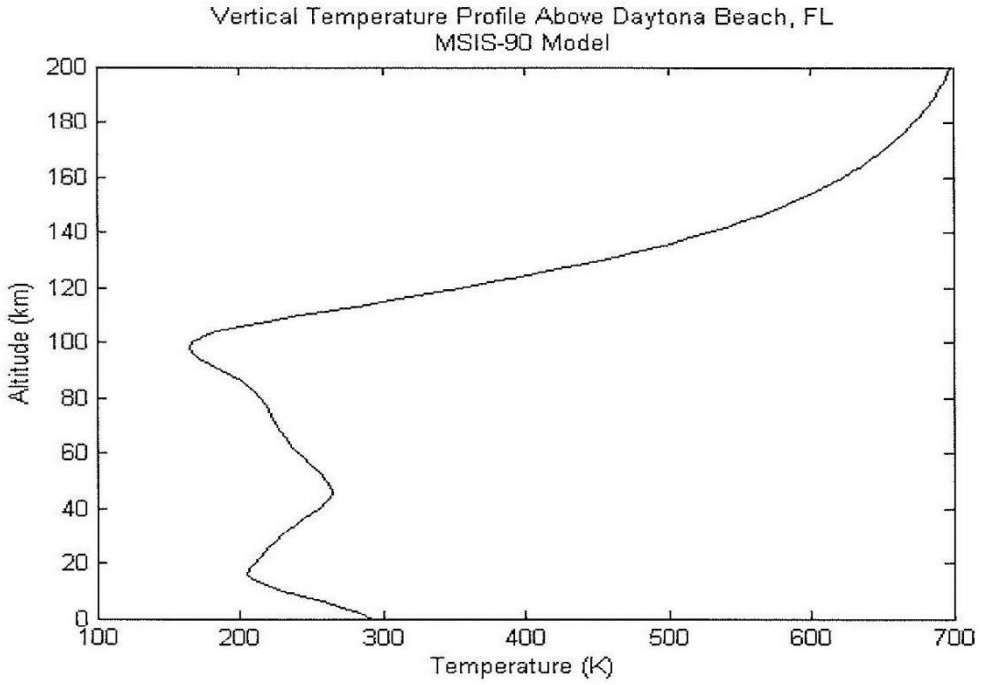

Figure 1.1: Vertical temperature profile above Daytona Beach, FL from the surface to an altitude of 200 km. [Hughes, 2008]

the pressure from the gas below balances the weight of the gas column above [Prolss, 2004, Cravens, 1997]. Using the ideal gas law, $P = nkT$, the hydrostatic equation, in terms of pressure becomes $P = P_0 e^{(-z/H)}$ where $H = kT/mg$, m is mass, g is the acceleration due to gravity, T is temperature, k is Boltzmann's constant, z is altitude, and P_0 is the pressure at the surface of Earth. Through the ideal gas law the hydrostatic equation can also be written in terms of mass and number density. The scale height, H, signifies the altitude range over which pressure, mass density, and number density decrease by a factor of $1/e$; this altitude is approximately 8 km at the surface of the Earth.

The vertical temperature profile is depicted in Figure 1.1. It is characterized by three maxima and two minima with connecting layers of increasing or decreasing

temperature in between. The first maxima occurs at the surface of the Earth where the temperature reaches about 293 K [MSIS 90 Model]. Most of the heat at the surface comes from the direct absorption of solar radiation with some heat coming from the reabsorption of Earth's own infrared radiation, reflected primarily from atmospheric water vapor [Prolss, 2004]. Above the Earth's surface radiative cooling causes the atmospheric temperature to decrease with increasing height. This layer of decreasing temperature is known as the troposphere. At an altitude of about 10 km, the temperature reaches a broad minimum, known as the tropopause. The temperature then rises again due to the absorption of ultraviolet solar radiation at wavelengths above 200 nm by the trace gas ozone (O_3) [Prolss, 2004, Tribble, 2003]. This layer is called the stratosphere and its upper boundary at roughly 50 km is called the stratopause which has a temperature close to that of the Earth's surface. Above the stratopause, radiative cooling becomes effective particularly due to the trace gas carbon dioxide [Prolss, 2004]. The layer of decreasing temperature is known as the mesosphere and reaches a minimum temperature at a height of 80–90 km. The upper boundary, known as the mesopause, generally has a minimum temperature of ~180 K [Tribble, 2003]. The thermosphere is the region of temperature increase above the mesopause. This dramatic temperature increase is due to the absorption of solar ultraviolet radiation at wavelengths below 200 nm by the ambient constituents [Tribble, 2003]. At heights above about 200 km, the temperature asymptotically approaches a limiting value which can vary between 600 K and 2500 K but is usually ~1000 K [Prolss, 2004]. In general, the lower atmosphere includes the troposphere, the middle atmosphere consists of the stratosphere and mesosphere, and the thermosphere defines the upper atmosphere.

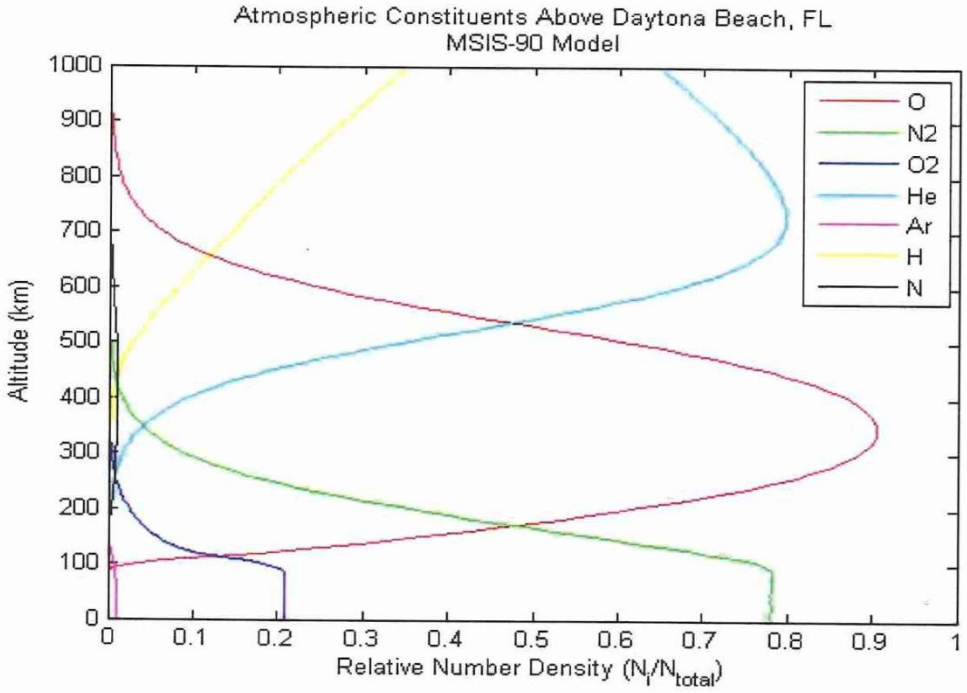

Figure 1.2: Relative particle density of the atmospheric constituents at various altitudes above Daytona Beach. [Hughes, 2008]

An alternate classification of the atmospheric regions is based on the atmospheric constituents. The relative number density for each constituent is constant below about 90 km. At higher altitudes the relative number densities for the atmospheric constituents vary significantly as seen in Figure 1.2. Below 90 km the atmosphere is well mixed due to turbulence and atmospheric eddy motions and is known as the homosphere [Cravens, 1997]. The homopause separates the homosphere and the heterosphere which is the region where atmospheric species gravitationally separate according to their individual scale heights, $H_i = kT_i/m_i g$ where i is the particular species. As a result, heavy gases will fall off rapidly and light gases gradually with height [Prolss, 2004, Cravens, 1997]. Dominant constituents at various altitudes are listed in the following table. From Table 1.1 it is interesting to note that atomic

Altitude Range	Dominant Constituent
0 - 180 km	N_2
180 - 700 km	O
700 - 1700 km	He
> 1700 km	H

Table 1.1: Dominant atmospheric constituent at different altitude ranges [Prolss, 2004].

hydrogen and atomic oxygen are not intrinsic constituents of the lower atmosphere but are both dominant in the upper atmosphere. Atomic oxygen is produced by the photodissociation of molecular oxygen O_2 where the dissociation products, depending on the photon energy, can occur in an excited state [Cravens, 1997, Prolss, 2004]. The significant atomic oxygen densities are due to the extremely slow loss process of three body collisional recombination. The mean life expectancy of an oxygen atom is therefore a few months at a height of 100 km and orders of magnitude longer at 150 km [Prolss, 2004]. Below 100 km however, the loss rate of atomic oxygen grows rapidly and the mean life expectancy of these particles drops to only a few hours at an altitude of 80 km. Like atomic oxygen, atomic hydrogen is produced only at greater heights due to the photodissociation of water molecules H_2 [Prolss, 2004].

For the purposes of this thesis, we are concerned with atomic oxygen and its dipole forbidden transition resulting in the production of the green line in the nightglow spectrum of the mesosphere/lower thermosphere region of the atmosphere.

1.2 5577 Å Line

Absorption of solar radiation at wavelengths less than 200 nm by the Earth's thermosphere leads to the excitation of neutral atoms and molecules and the resulting

emission of "nightglow" photons as the excited constituents relax to lower energy states. The green emission line of excited atomic oxygen ($^1S_0 \rightarrow {}^1D_2$) at 5577 Å is the brightest emission line in the visible region of the nightglow spectrum with an average nightglow intensity of 250 Rayleighs and a maximum intensity during the middle hours of the night [Chattopadhyay and Midya, 2006, Roach, 1954]. This "forbidden" transition originates from two distinct layers, one in the F-region of the ionosphere at about 250–300 km, the other in the lower thermosphere around 95–100 km [Rees, 1989].

The excitation mechanism of $O(^1S_0)$ which is responsible for the 5577 Å emission is a two-step energy transfer mechanism, the first of which is the following three-body reaction:

$$O + O + M \rightarrow O_2^* + M$$
$$O_2^* + O \rightarrow O_2 + O(^1S_0)$$
$$O(^1S_0) \rightarrow O(^1D_2) + h\nu_{(\lambda=5577\mathring{A})}$$

where O_2^* indicates an excited state of O_2 and M is an arbitrary three-particle collision partner [Gobbi et al., 1992].

Through the reactions, models and observations show that the green line volume emission rate profiles peak near 96 km [Gobbi et al., 1992, Melo et al., 1996]. Due to its brightness and altitude of the peak volume emission rate, the 5577 Å green line can be used to measure the neutral winds of the upper mesosphere/lower thermosphere which is a region of significant dynamic complexity and variability.

1.3 Atmospheric Dynamics

Above 80 km, the atmosphere displays a wide range of dynamical phenomena, largely hydrodynamic in nature. The dynamics of the upper atmosphere, more specifically the mesosphere and lower thermosphere region are governed by a number of external processes resulting in a complex and variable region. On a global average, the dominant heat source below 150 km to about 100 km is O_2 absorption in the Schumann-Runge continuum (130–175 nm) [Roble, 1995, Fuller-Rowell, 1995]. The diurnal and latitudinal variations of this heat input creates global scale pressure gradients which set the atmosphere in motion. As the atmosphere is set in motion the Coriolis force begins to act, moving gas in a clockwise sense in the northern hemisphere and counter-clockwise in the southern hemisphere. The action of Earth's rotation trying to balance the pressure gradients produced by heating is known as the geostrophic balance, one of the most fundamental relationships in atmospheric dynamics [Fuller-Rowell, 1995, Prolss, 2004]. This geostrophic approximation is a good approximation for the motion of neutral gas in the upper troposphere and stratosphere. In the mesopause region, however, ion drag and viscosity terms enter the equations of motion.

Collisions between ions and neutrals in the thermosphere are frequent enough that they affect each other. If no electric field is present, ions act to slow the neutral winds. On the other hand, with the presence of an electric field, collisions between ions and neutral particles can result in the acceleration of the neutral winds to velocities of several hundred of meters per second [Fuller-Rowell, 1995, Rees, 1989]. The collisional interaction between neutral and plasma components is represented by the ion-drag term.

A notable characteristic of the lower thermosphere is the transition from turbulent

mixing to molecular diffusion. A steep vertical shear results from this cross-over and partly causes the high degree of vertical structure in this region. The viscosity term acts to smooth gradients in the wind field, particularly over short vertical distances [Fuller-Rowell, 1995].

The balance of these four main forces, pressure gradients, the resulting Coriolis force, ion drag and viscosity; is described by the following equation of motion

$$\frac{D}{Dt}V = -\frac{1}{\rho}\nabla P - 2\Omega \times V - \nu_{ni}(V - U) + \frac{1}{\rho}\nabla(\mu \nabla V), \tag{1.1}$$

where V is the neutral wind velocity, P is the neutral gas pressure, Ω is the angular velocity of Earth, U is the ion drift velocity, ν_{ni} is the neutral-ion collision frequency, ρ is the neutral gas density, and μ is the sum of the molecular and turbulent viscosity coefficient [Fuller-Rowell, 1995]. In Earth's frame, where latitude and longitude are the independent variables, the change in velocity of the southward or meridional (V_θ) and the eastward or zonal (V_ϕ) wind components are given by

$$\frac{\partial}{\partial t}V_\theta = \frac{V_\theta}{r}\frac{\partial}{\partial \theta}V_\theta - \frac{V_\phi}{r\sin\theta}\frac{\partial}{\partial \phi}V_\theta - V_z\frac{\partial}{\partial z}V_\theta + \left(2\Omega + \frac{V_\phi}{r\sin\theta}\right)V_\phi \cos\theta +$$

$$\frac{1}{\rho}\frac{\partial}{\partial z}\left(\mu\frac{\partial}{\partial z}V_\theta\right) - \nu_{ni}(V_\theta - U_\theta) - \frac{1}{\rho r}\frac{\partial}{\partial \theta}P \tag{1.2}$$

and

$$\frac{\partial}{\partial t}V_\phi = \frac{V_\theta}{r}\frac{\partial}{\partial \theta}V_\phi - \frac{V_\phi}{r\sin\theta}\frac{\partial}{\partial \phi}V_\phi - V_z\frac{\partial}{\partial z}V_\phi + \left(2\Omega + \frac{V_\phi}{r\sin\theta}\right)V_\theta \cos\theta +$$

$$\frac{1}{\rho}\frac{\partial}{\partial z}\left(\mu\frac{\partial}{\partial z}V_\phi\right) - \nu_{ni}(V_\phi - U_\phi) - \frac{1}{\rho r}\frac{\partial}{\partial \phi}P, \tag{1.3}$$

where r is Earth's radius, θ is co-latitude, ϕ is longitude, and z is altitude [Fuller-Rowell, 1995].

In addition to the fluid dynamics which govern the motion of the atmosphere, a wide range of atmospheric waves propagate from a number of different sources in the lower atmosphere. Among these are tides, planetary waves and gravity waves which are major dynamical phenomena and sources of energy that interact in the mesosphere and lower thermosphere. The tendency of the amplitude of tidal or wave velocity to increase with increasing height is characteristic of tides and internal atmospheric waves [Hines, 1962]. This enhancement in velocity is due to the conservation of energy. As the gas density decreases with altitude, the only way for the energy flux to remain constant as the tide or wave propagates upward is if the amplitude of the oscillating velocity vector increases. Because of this intrinsic enhancement, tidal oscillations and other internal waves can play a major role in the dynamics of the upper atmosphere.

Tides are global-scale harmonic variations with periods of a day or fraction of a day. These oscillations are excited thermally or gravitationally [Hines, 1962]. Lunar tides are generated gravitationally and have periods of 12 lunar hours. The more dominant solar tides are generated thermally and are classified as migrating and non-migrating solar thermal tides. Migrating tides mainly travel westward with the Sun and are produced by the heating of ozone in the stratosphere and water vapor in the troposphere. Sources of non-migrating tides which do not follow the Sun include Earth's topography and the latent heat release of water vapor. Produced efficiently by tropospheric sources, the migrating solar diurnal tide has a period of 24 hours and is primarily confined to lower latitudes [Fritts, 1995b]. The migrating solar semi–diurnal tide on the other hand propagates at all latitudes and has a large vertical

wavelength efficiently generated by ozone heating. The dominant tidal modes are produced by ozone heating and have periods which are integral subharmonics of a solar day: 24 hr, 12 hr, 8 hr, 6 hr,$\cdots$ [Fuller-Rowell, 1995, Fritts, 1995b].

Planetary waves are also global scale atmospheric waves forced by features at Earth's surface such as mountains, large land masses, and meteorological patterns. These waves propagate vertically into the stratosphere and mesosphere. Planetary waves with periods of 2, 5, 10, and 16 days have been documented in the mesosphere and lower thermosphere. [Fritts, 1995b]

Atmospheric gravity waves are irregular components superimposed on the prevailing and tidal winds. Their magnitude is comparable to that of tides but on a time scale of only an hour or so [Hines, 1962]. Sources of gravity waves include airflow over topography, convective storms, and other tropospheric features such as frontal activity. The nature of the source and the various dissipation processes of gravity waves results in highly variable outcomes and can be important drivers of dynamical change in the mesosphere as well as in the lower thermosphere. For these reasons and because observations of gravity waves are central to the results presented in this thesis, they will be considered in more detail.

1.3.1 Atmospheric Gravity Waves

Gravity waves are oscillations created by the lifting of fluid buoyancy and the restoring force of gravity. Figure 1.3 illustrates the harmonic motion of an air parcel which has been displaced from its equilibrium position. Consider a parcel of air displaced a small distance upward from its equilibrium position in an atmosphere at rest. Assuming the parcel does not mix with its surroundings while displaced and that the process is

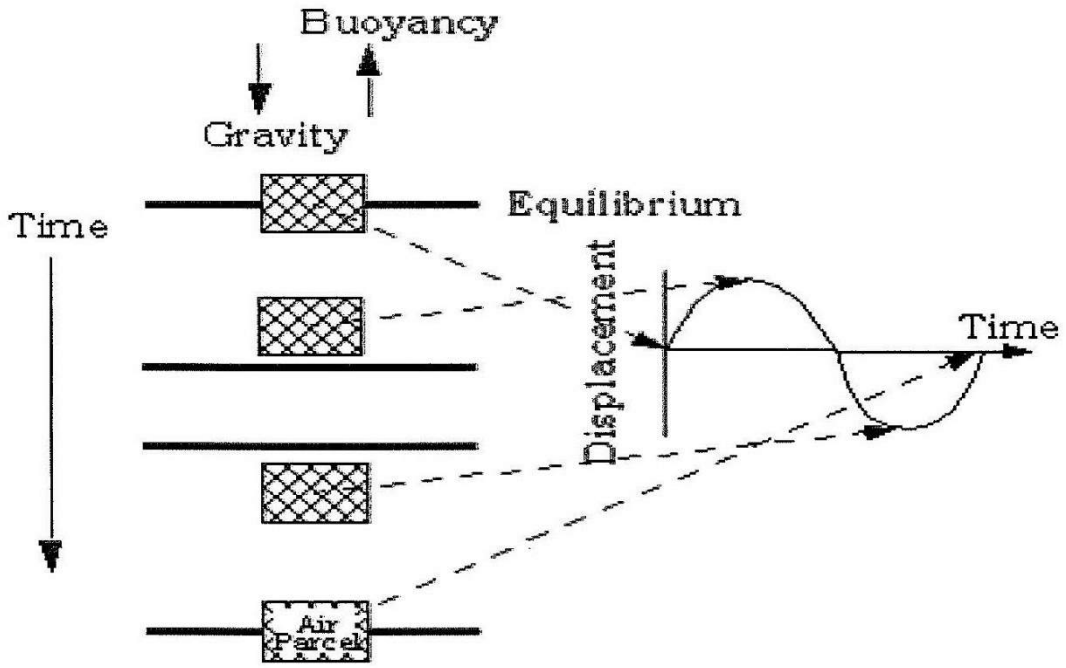

Figure 1.3: Diagram of the behavior of a gravity wave. Fluid buoyancy acts as the restoring force when an air parcel is displaced. [http://sprg.ssl.berkeley.edu/atmos/gj_science.html]

adiabatic, gravity will act as a restoring force on the parcel. Accelerating the displaced air parcel toward Earth, the force of gravity will cause the parcel to overshoot its equilibrium position. The air parcel is now in a denser medium than its equilibrium surrounding; therefore more buoyant than its environment. Fluid buoyancy acts on the air parcel to lift it back in its equilibrium state. The vertical buoyant force acting on the air parcel is

$$\vec{F_b} = -g(m_p - m_a)\hat{z}, \tag{1.4}$$

where m_a is the mass of the air displaced by the fluid parcel, m_p is the mass of the fluid parcel, and g is the acceleration due to gravity [Nappo, 2002]. Applying the

ideal gas law, this force can also be expressed as

$$\frac{d^2(\delta z)}{dt^2} = -g\frac{\rho_p - \rho_a}{\rho_p} = -g\frac{T_a - T_p}{T_a}, \tag{1.5}$$

where ρ_p is the density of the air parcel with temperature T_p displaced upward by the distance δz, ρ_a is the environmental air density, T_a is the environmental temperature and g is the acceleration due to gravity. Expanding T_a and T_p to the first order,

$$T_a(z_e + \delta z) = T_0 + \left.\frac{\partial T_a}{\partial z}\right|_{z_e} \delta z + ... \tag{1.6}$$

$$T_p(z_e + \delta z) = T_0 + \left.\frac{\partial T_p}{\partial z}\right|_{z_e} \delta z + ..., \tag{1.7}$$

where T_0 is the temperature at equilibrium height z_e. Taking note that the change of environmental temperature due to the vertical displacement is small [Nappo, 2002], equation (1.5) becomes

$$\frac{d^2(\delta z)}{dt^2} = -\frac{g}{T_a}\left(\frac{\partial T_a}{\partial z} - \frac{\partial T_p}{\partial z}\right)\delta z = -N^2\delta z \tag{1.8}$$

which is an example of simple harmonic motion and therefore the air parcel's motion when displaced vertically and is released becomes

$$\delta z(t) = Ae^{iNt} + Be^{-iNt}, \tag{1.9}$$

where N is known as the Brunt-Väisälä frequency if real. N is usually represented in terms of the potential temperature which is the temperature an air parcel would have if it were brought down adiabatically from a height where the pressure is p to a

height where the pressure is 1000 mb [Nappo, 2002]. The potential temperature, Θ is defined as

$$\Theta = T_a\left(\frac{1000}{p}\right)^{\frac{R}{c_p}}, \tag{1.10}$$

where R is the gas constant, c_p is the specific heat at constant pressure, and p is the pressure at which the air parcel is originally. Using the ideal gas law and the hydrostatic approximation and taking the logarithmic derivative of the potential temperature, Θ, the Brunt-Väisälä frequency can be written as

$$N = \sqrt{\frac{g}{\theta}\frac{\partial\theta}{\partial z}}. \tag{1.11}$$

If N is imaginary, $\partial\theta/\partial z < 0$, instability is produced and the solution would represent unbounded growth of the displacement. When $\partial\theta/\partial z = 0$, the buoyancy period is on the buoyancy period is five to eight minutes given an isothermal atmosphere. Wave motion is possible only if the atmosphere is stably stratified, when $\partial\theta/\partial z > 0$. However, N is not always the frequency of the gravity wave, it instead represents the maximum frequency for vertically propagating gravity waves.

The previous derivation was for air parcels that are vertically displaced only; however, gravity waves almost always propagate at some angle to the vertical. In the case of off-vertical propagation, the buoyancy force acting on the displaced air parcel becomes

$$\vec{F_s} = m_p\frac{d^2(\delta s)}{dt^2} = -g\sin\beta(m_p - ma), \tag{1.12}$$

where δs is the displacement of an air parcel from its equilibrium position on a surface inclined at an angle β from the horizontal. Following the same derivation steps as for the vertical case, the motion of the parcel propagating at an angle to the vertical,

along the s-direction is

$$\delta s(t) = Ae^{iN't} + Be^{-iN't}, \tag{1.13}$$

where

$$N' = \sqrt{\frac{g}{\theta}\frac{\partial\theta}{\partial z}\sin^2\beta} = N\sin\beta. \tag{1.14}$$

The range of buoyancy frequencies extends from 0 to N depending on the angle of propagation relative to the horizontal plane, β [Nappo, 2002].

In terms of the equations of motion for an irrotational, frictionless atmosphere, atmospheric oscillations with perturbation magnitude are governed by the following set of equations:

$$\rho_0\left(\frac{\partial\vec{U}}{\partial t}\right) = \rho g - \nabla P \tag{1.15}$$

$$\frac{\partial P}{\partial t} + \vec{U}\cdot\nabla P_0 = C^2\left[\frac{\partial\rho}{\partial t} + \vec{U}\cdot\nabla\rho_0\right] \tag{1.16}$$

$$\frac{\partial\rho}{\partial t} + \vec{U}\cdot\nabla\rho_0 + \rho_0(\nabla\cdot\vec{U}) = 0, \tag{1.17}$$

where $\vec{U}$ is the perturbation velocity, P is the perturbed atmospheric pressure, ρ is the perturbed atmospheric density, P_0 is the unperturbed atmospheric pressure, ρ_0 is the unperturbed atmospheric density, g is the acceleration due to gravity, and C is the speed of sound [Hines, 1960, Nappo, 2002]. Equations 1.15, 1.16 and 1.17 represent the conservation of momentum, the conservation of thermal energy, and the conservation of mass, respectively. The wave solutions of the set of equations (1.15–1.17) will take the form

$$u(x,y,z,t) = \tilde{u}e^{(kx+ly+mz-\omega t)} \tag{1.18}$$

where $\tilde{u}$ is the complex amplitude, k, l, and m are the wave numbers in the x, y, and z–directions, respectively, and ω is the angular frequency of the wave. From the plane wave equation (1.18), various properties and relations characteristic to gravity waves have been formed.

1.4 Motivation

Atmospheric gravity waves have been recognized as essential parts of the dynamics of the atmosphere on all meteorological scales. Their ability to transport momentum and energy away from the disturbances that generate them and distribute this energy throughout the atmosphere is an important component of atmospheric dynamics. The transported energy increases by a factor of about 100 from the troposphere to the mesosphere which makes them significant in the lower thermosphere region [Fritts, 1995a]. Not only do they contribute the majority of the energy and momentum fluxes above the stratosphere, their wave dissipation causes flux divergences which lead to local heating, turbulent diffusion, and accelerations of the local mean flow [Fritts, 1995a]. It is also reasonably conclusive now that the breaking of gravity waves in the mesopause region results in the observed temperature increase toward the winter pole [Hines, 1960]. The strong dynamical coupling between the lower and upper atmospheric regions that gravity waves govern makes it necessary to study them in order to better characterize and understand the atmosphere in its entirety.

The most studied source of atmospheric gravity waves has been airflow over topography. Another significant source however is convection in the troposphere. Gravity waves produced by thunderstorms have been previously observed using microbarographs and can have a wide range of periods [Jordan, 1972, Curry and Murty, 1974,

Balachandran, 1980]. M.J. Taylor et al. [1995] observed gravity waves generated by thunderstorms by imaging the hydroxyl nightglow emission and reported periods of less than an hour. Radar observations have also led to the identification of gravity waves from thunderstorms [Hansen et al., 2002]. This thesis will present Fabry–Perot interferometer observations of neutral winds at 96 km and will discuss observations of gravity wave activity which correlates with active thunderstorms.

Chapter 2

Instrumentation

2.1 Fabry-Perot Interferometer

Fabry-Perot interferometers have been utilized to observe the neutral winds for many years [Ishii et al., 1999, Griffin et al., 2008, Biondi et al., 1995, Meriwether et al., 1997, Shiokawa et al., 2003, Vila et al., 1998]. Their characteristic high throughput and resolving power make them a favorable instrument to detect small Doppler shifts in atmospheric emissions [Ishii et al., 1997].

A Fabry-Perot interferometer (FPI) is an optical instrument which uses multiple-beam interference to create an interference pattern. A high throughput FPI will be used to detect Doppler shifts on the order of 10^{-4} nm in the faint nightglow. Embry-Riddle Aeronautical University's (ERAU) Space Physics Research Laboratory (SPRL) possesses a FPI housed in the attic of the Lehman Engineering and Technology Center on the Daytona Beach, FL campus. The following two sections will discuss the general theory behind a FPI with an etalon of a fixed spacing like the one at ERAU and ERAU's FPI in detail.

2.1.1 Theory of a Fabry-Perot Etalon

The core of an FPI is an etalon, two highly reflective parallel surfaces separated by some small distance. Consider the etalon with a spacing of l between the two surfaces in Figure 2.1. A light ray is incident on the first surface at point A at an angle θ_i from the horizontal. The light ray is partially transmitted and partially reflected at the first surface. The component of the ray which is transmitted refracts as it enters the etalon to an angle θ_e due to Snell's Law. This ray will then traverse the etalon to point B where the ray will again be partly transmitted and partly reflected. The transmitted part, T_1, will exit the etalon at B at an angle θ_i while the division process of the reflected component will continue. The following transmitted ray, T_2 leaves the etalon at point D at an angle θ_i from the normal. It is clear that the ray labeled T_2 has traveled a longer optical path than the ray labeled T_1.

The optical path difference between the two consecutive transmitted rays is equal to the two additional trips T_2 makes across the etalon minus the extra distance T_1 must travel to match the progress of T_2 along the second surface of the etalon [Pedrotti et al., 2007]. In relation to Figure 2.1, the optical path difference is given as

$$\delta_{PD} = n_e(BC + CD) - n_i(BF), \tag{2.1}$$

where n_e is the index of refraction of the medium between the two surfaces of the etalon and n_i is the index of refraction of the medium surrounding the etalon. Segments BC and CD are equivalent and can be written as

$$BC = CD = \frac{l}{\cos\theta_e}. \tag{2.2}$$

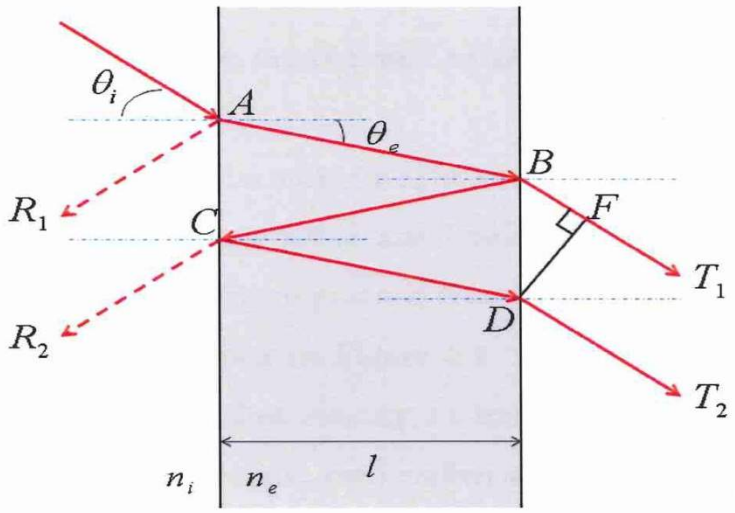

Figure 2.1: Path of a light ray through a Fabry-Perot etalon.

It can be shown that segment BF is

$$BF = BD \sin\theta_i = \frac{2l}{\cos\theta_e} \sin\theta_e \sin\theta_i. \tag{2.3}$$

The optical path difference in terms of the given parameters in Figure 2.1 becomes

$$\delta_{PD} = n_e\left(\frac{2l}{\cos\theta_e}\right) - n_i\left(\frac{2l}{\cos\theta_e}\sin\theta_e \sin\theta_i\right). \tag{2.4}$$

Applying Snell's Law, Equation 2.4 can be simplified to

$$\delta_{PD} = \frac{2l}{\cos\theta_e}(n_e - n_e \sin^2\theta_e) = \frac{2ln_e}{\cos\theta_e}(1 - \sin^2\theta_e) = 2ln_e \cos\theta_e. \tag{2.5}$$

For constructive interference to occur, the optical path difference must equal an integer multiple of the wavelength, i.e., $\delta_{PD} = m\lambda$ where $m = 0, \pm 1, \pm 2, \cdots$. On the other hand, for destructive interference to occur, $\delta_{PD} = (m + 1/2)\lambda$ where $m = 0, \pm 1, \pm 2, \cdots$.

A FPI creates a pattern of alternating bright and dark concentric rings, or fringes. Bright rings result from the constructive interference and dark fringes are produced by destructive interference. A fringe pattern created by the 5577 Å green line after filtering by ERAU's FPI is shown in Figure 2.2. If the distance between the two surfaces of the etalon is such that exactly m half–wavelengths of light fit in the etalon, a bright spot of order m and zero radius where $\theta_i = \theta_e = 0$ would appear. This corresponds to the central order of interference [Hernandez, 1986]. In general, however, the spacing l does not allow exactly m number of half-wavelengths to fit inside the etalon which results in the central order fringe occurring at some small nonzero angle and having a nonzero radius as seen in Figure 2.2.

The fundamental behavior of a FPI is the appearance of a single wavelength,λ, a multiple number of times at specific angles given by

$$\lambda m = 2ln_e \cos\theta. \tag{2.6}$$

As the incident angle increases from zero degrees, the interference becomes destructive then constructive when the path difference decreases by a full wavelength, i.e. when θ_i increases to say θ_1. This occurrence of constructive interference corresponds to the first bright ring from the center in both images in Figure 2.2. The interference is constructive from any point along the circle described by θ_1 and therefore a concentric fringe results. The order of this fringe is the $(m-1)$ fringe since δ_{PD} was reduced as

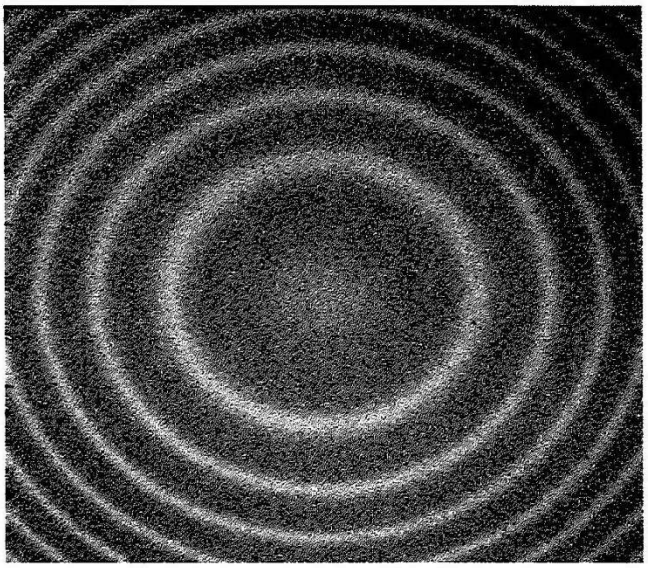

Figure 2.2: Fringe pattern produced by the 5577 Å green line after filtering by the ERAU Fabry–Perot.

the angle increased [Hernandez, 1986]. Further increase of the incident angle results in successive concentric fringes where the k^{th} fringe from the center has an order $(m-k)$.

An important property which characterizes a FPI is its free spectral range (FSR). The FSR is the wavelength separation between adjacent transmission peaks [Pedrotti et al., 2007]. A change in wavelength of one FSR shifts a fringe of a given order onto the next successive fringe. To find the FSR in terms of wavelength, consider two wavelengths which appear at the same angle, θ, but have orders of interference that differ by one, $\lambda_m = \frac{2ln_e\cos\theta}{m}$ and $\lambda_{(m-1)} = \frac{2ln_e\cos\theta}{(m-1)}$. The difference in wavelength becomes

$$\lambda_m - \lambda_{(m-1)} = \triangle\lambda = \frac{2ln_e\cos\theta}{m} - \frac{2ln_e\cos\theta}{m-1} = \frac{-2ln_e\cos\theta}{m^2-m}. \tag{2.7}$$

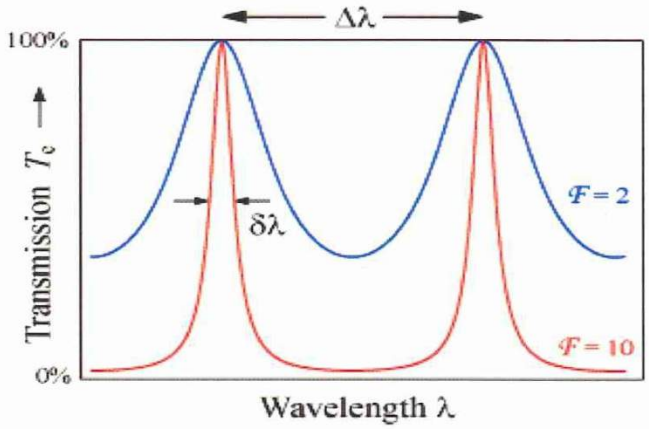

Figure 2.3: Example of a Fabry-Perot transmission profile. The plot is of transmittance and wavelength for selected values of $\mathcal{F}$. The free spectral range is given as $\triangle\lambda$ and the FWHM is labeled as $\delta\lambda$. [`http://www.scientific-web.com/en/Physics/Optics/FabryPerotInterferometer.html`]

For small angles, equation 2.7 can also be written as

$$\triangle\lambda = \frac{\lambda^2}{2l}, \tag{2.8}$$

where, as previously mentioned, l is the spacing between the two plates of the etalon and λ is the wavelength of the radiation [Hernandez, 1986]. The ratio of the FSR in wavelength to the full–width at half–maximum (FWHM) of the transmittance peaks is known as the finesse, $\mathcal{F}$. Etalons with a higher finesse show sharper transmission peaks than those with a lower one. Figure 2.3 displays the difference in transmittance peak curves for two different values of finesse. It is clear the curve with the higher finesse value has sharper transmittance peaks. Another point to note, the higher finesse value corresponds to a higher reflectivity; the higher the reflectivity of the surfaces of the etalon, the higher the finesse.

2.1.2 ERAU's Fabry-Perot

SPRL at ERAU possesses a FPI with an overall finesse of approximately 3.4. SPRL's FPI contains a temperature–stabilized etalon with a large diameter of 15 cm which essentially equates to a high throughput FPI. The medium between the top and bottom plates spaced 20.49 mm apart is air ($n = 1$). The night sky is viewed at an elevation angle of 30° through an optical dome. A clockwise rotating mirror views the night sky at four different azimuths, north, south, east and west. One 2–bit light sensor is placed on the rotating piece of the scanning mirror to allow for its orientation to be computer–controlled. Small pieces of silver and/or black colored tape are placed on the rotor mount at the four cardinal directions so that the light sensor can detect the position of the mirror. The radiation from the night sky reflects off the mirror toward the etalon and then passes through a 557.7 nm transmission filter and a mechanical shutter. The mechanical shutter is closed while the mirror rotates and is opened when the mirror is positioned in the desired orientation. While the shutter is open, the Andor DU434 1024x1024 back-illuminated CCD array is exposed to the filtered atmospheric radiation. With an image area of 13.3x13.3 mm, the detector is continuously thermoelectrically cooled to −50° C. Figure 2.4 is a picture of SPRL's FPI on the top floor of ERAU's Lehman Engineering and Technology Center in Daytona Beach, FL.

Two optical lenses are also included in ERAU's FPI configuration which work as a telescope to focus the interference pattern emerging from the etalon onto the CCD detector. One lens is directly below the etalon and the second lens is placed after the filter.

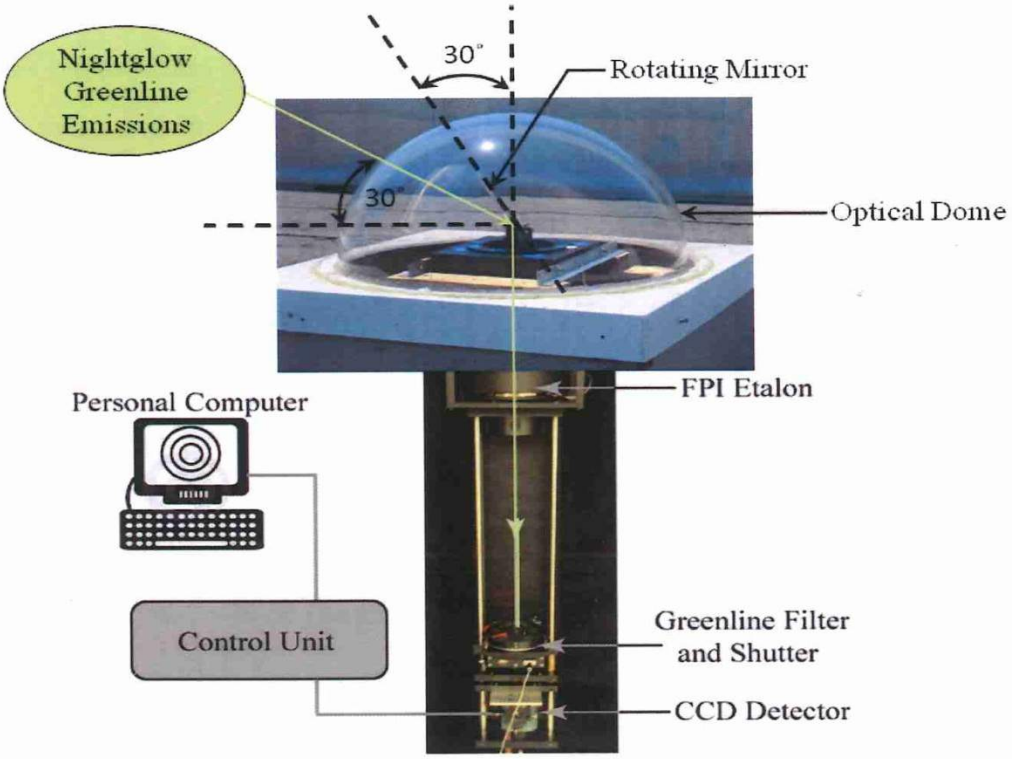

Figure 2.4: Configuration of the FPI at ERAU. [Hughes, 2010]

2.2 Measurement Technique

Measurements taken by the FPI at ERAU begin at nautical twilight, when the solar depression angle is $-12°$. A program written in Andor is used to calculate this angle each day automatically. Once the Sun has dropped below the horizon by 12°, the mirror is rotated clockwise to face north. At this time, the shutter will open and the CCD will be exposed for 300 seconds. After 300 seconds the shutter closes and the image is read out from the CCD to the computer which takes approximately 17 seconds. A cushion time of three seconds is written into the Andor program so the mirror will not rotate for 20 seconds after the shutter closed. The mirror then moves 180° to face south. The time for this rotation is about 14 seconds; again, some cushion time is written into the program so that the shutter will open 20 seconds after the initial movement of the mirror from north. The integration time and read out time is the same for all scans, 300 seconds and 17 seconds, respectively. Following the read out time of the image produced while the mirror is facing south the mirror rotates 270° to face east which takes an estimated 21 seconds. The shutter will open 25 seconds after the mirror begins to move from the south position. The mirror then turns 180° to face west; an image is taken and read out. Twenty seconds after the image is read out the mirror will rotate 90° to face north and the same procedure is repeated continuously throughout the night until the Sun rises to 12° below the horizon.

To determine the horizontal neutral winds in two dimensions, consecutive north and south scans are used together to determine the meridional component while the zonal component is extracted from consecutive east and west scans. The reason for the order of rotation of the mirror mentioned in the previous paragraph is to optimize

the temporal resolution of the winds. A short integration time of 300 seconds for each image also improves the time resolution of the time series of the meridional and zonal winds which will be produced from the scans taken throughout the night. With the exposure time and rotation order, a temporal resolution of about 11 minutes is achieved.

Chapter 3

Data Analysis Technique

3.1 Determining the Horizontal Winds

The FPI at SPRL outputs a fringe pattern of six concentric rings for every 300 second scan. This image is then transformed into a transmission profile for data analysis use. The profile is in terms of radius–squared CCD pixels with evenly spaced peaks. To obtain this profile the center of the image must be known. The center is found using a MATLAB GUI developed by Dr. John Hughes . The pixel count is then averaged in concentric rings of integer radii around that center. In the raw image the distance between the concentric bright rings decreases away from the center. It can be shown that for small angles, the radius of a fringe ordered m varies as $(m_c - m)^{1/2}$, where m_c is the central order; therefore squaring the radial index results in the distance between the peaks being equal. Figure 3.1 depicts a raw image (left) and its corresponding radius–squared fringe profile (right). The y–axis of the fringe profile represents the average intensity at each radius and is in arbitrary units. Six peaks are seen in the radius–squared fringe profile; these peaks are in accord with the six bright concentric

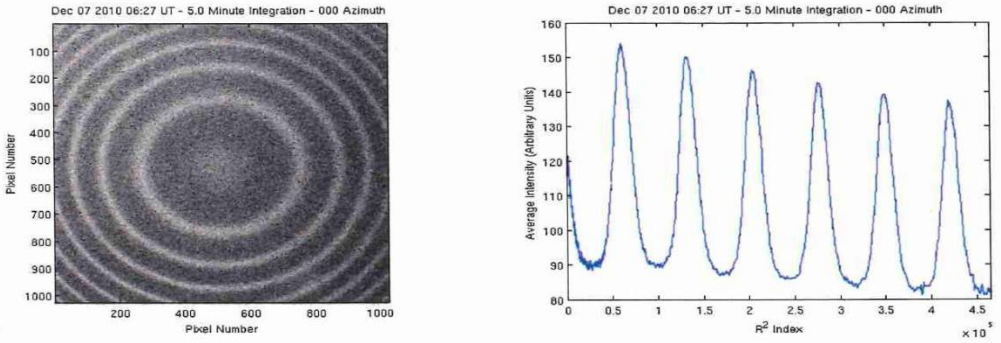

Figure 3.1: SPRL FPI image (left) of nightglow greenline emission from the north direction and corresponding radius–squared fringe pattern (right). The image was taken on Dec 07, 2010 with an integration time of 5 minutes beginning at 06:27 UT.

circles which represent the orders of constructive interference. The troughs of the profile depict the occurrence of destructive interference.

To compute the horizontal winds at an altitude of 96 km, the Doppler shift of the atomic oxygen green line must be determined. From a ground based instrument, like SPRL's FPI, and the assumption that the velocity is much smaller than the speed of light, c, the green line will be Doppler shifted by the line-of-sight (LOS) component of the neutral wind velocity vector (v_{LOS}) according to

$$\frac{\triangle f}{f} = -\frac{\triangle \lambda}{\lambda} = \frac{v_{LOS}}{c}, \tag{3.1}$$

where f and λ are the frequency and wavelength of the green line emission, respectively, and $\triangle f$ and $\triangle \lambda$ are the frequency Doppler shift and wavelength Doppler shift of the green line, respectively. In order to calculate the LOS velocity using equation 3.1, the observed wavelength must be known. The observed wavelength can be found using equation 2.6 however, the angle θ of a given order is not measured with the FPI; therefore, a different method is used which involves the FSR.

As previously explained a change in wavelength of one FSR shifts a fringe of a given order onto the next successive fringe. This occurs for the greenline when there is a LOS velocity equal to 4080 m/s, i.e.

$$v_{LOS_{FSR}} = \frac{\triangle\lambda}{\lambda}c = \frac{\frac{\lambda^2}{2l}}{\lambda}c = 4080m/s, \tag{3.2}$$

where λ is the wavelength of the green line, l is the spacing between the two plates of the etalon, and $\triangle\lambda$ is the change in wavelength corresponding to one FSR. If given a zero–wind radius–squared reference profile, the zero–wind FSR can be determined as well as the Doppler shift from the zero–wind reference profile in radius–squared CCD pixels. The v_{LOS} then can be found by

$$v_{LOS} = v_{LOS_{FSR}}\frac{\triangle(r^2)}{\triangle(r^2_{FSR})} = 4080\frac{\triangle(r^2)}{\triangle(r^2_{FSR})}m/s, \tag{3.3}$$

where $\triangle(r^2)$ is the shift from the zero–wind reference profile in units of radius–squared CCD pixels and $\triangle(r^2_{FSR})$ is the measured zero–wind FSR in the same units.

There are a number of ways to acquire the zero–wind reference profile. J.W. Meriwether et al. [1997] and P. Vila et al. [1998] used a set of zenith position scans as a measure of the zero–velocity position. This technique assumes that the vertical wind is negligible. P. Vila et al. [1998] describes a different method in which long–term observations of the horizontal winds in all directions are averaged to produce a zero–velocity wind profile under the assumption that the long–term divergence of the horizontal winds is small. Another approach uses a calibration source at or near the observing wavelength and in a sense "maps" the line positions of the wavelengths to obtain a zero–wind reference profile [Vila et al., 1998, Meriwether et al., 1997].

A fourth method is to take an average of two time–sequential profiles of opposite directions (N–S and E–W) to gather a zero–wind profile [Shiokawa et al., 2003]. This approach makes the assumption that there is no vertical wind and the horizontal wind is uniform in the viewing area of the FPI and over the time period of the two scans being averaged.

The first technique described is not practical for the current set up of the FPI at SPRL; nor is the third as there are not readily available calibration sources for a wavelength of 5577 Å . SPRL's FPI has been in operation for a short time and therefore has not yet gathered a large amount of data necessary to generate a long–term average. Consequently, the last of these methods will be used to produce the zero–wind reference profile.

Consider two time–sequential radius–squared profiles, one profile with a looking direction of north and the other profile with a looking direction of south (Figure 3.2). The zero–wind reference profile would be the average of these two. That is to say, the peaks of the reference profile would fall at the midpoint of the two profiles from opposite directions. Accordingly, the FSR of the zero–wind reference profile would be the difference between two peaks of consecutive order ($\triangle(r^2_{FSR})$). The shift from the reference profile at a specific order is then the difference between the peak of the zero–wind profile at a given order and the peak of one of the directional profiles at that same order ($\triangle(r^2)$) as seen in Figure 3.3.

3.1.1 Fitting the Peaks

To obtain numeric values for the shift from the zero-wind reference profile and the FSR, the center of the transmission peaks in units of radius–squared CCD pixels of

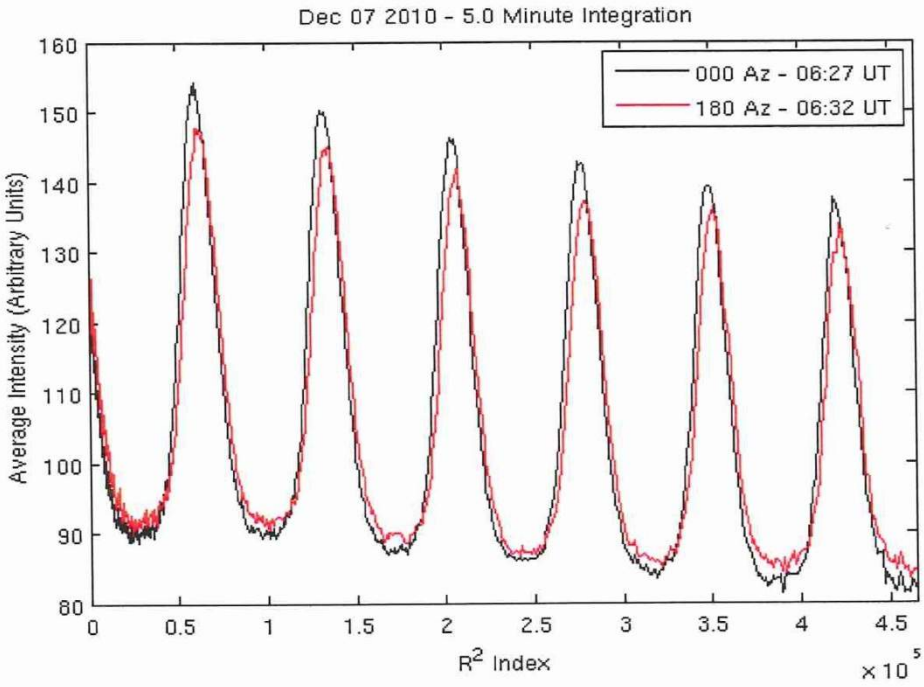

Figure 3.2: Two time-sequential radius–squared profiles of opposite directions extracted from images taken on Dec 07, 2010.

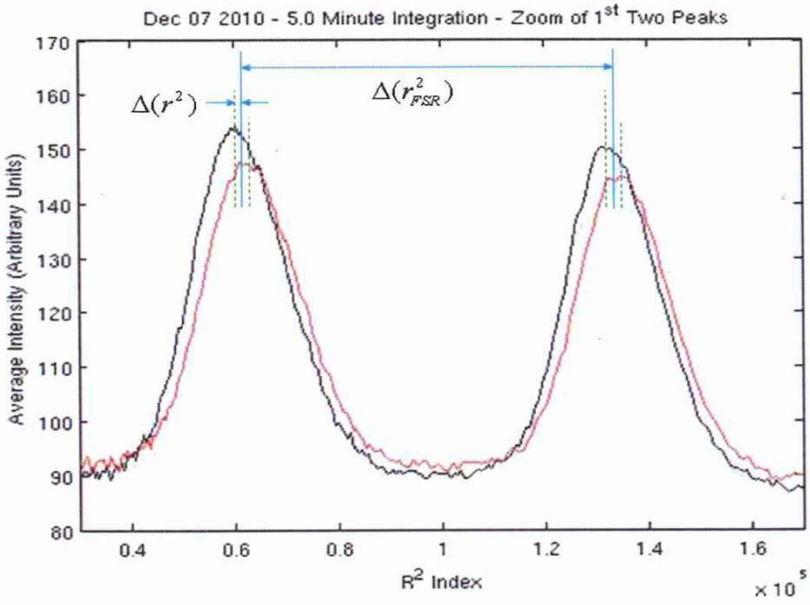

Figure 3.3: Enlarged image of the first two peaks from previous figure with $\triangle(r^2)$ and $\triangle(r^2_{FSR})$ labeled.

each directional profile must be known. A Gaussian function with a linear term is fitted to each peak to determine their centers. The equation for a Gaussian curve with a linear term is as follows

$$f(x) = Ae^{\frac{-(x-x_0)^2}{2\sigma^2}} + ax + b, \tag{3.4}$$

where A is the amplitude or height of the curve's peak, x_0 is the position of the center of the peak, σ^2 is the variance which determines the width of the curve, and $ax + b$ is the linear term. In the linear term, a is the slope of the line in which the Gaussian curve peaks from and b is the linear line's y–intercept. The method of steepest descent is used to determine the constants A, x_0, σ, a, and b.

The steepest descent method searches for the minimum of an N–dimensional function in the direction of a negative gradient

$$-g(x) = -\nabla f(x) = -\left[\frac{\partial f(x)}{\partial x_1}\frac{\partial f(x)}{\partial x_2}\cdots\frac{\partial f(x)}{\partial x_N}\right]^T, \tag{3.5}$$

[Yang et al., 2005]. The minimum of the reduced chi square function is to be found using this method and will in turn give the constants or, parameters which correspond to the best fit Gaussian curve. A reduced chi square value describes how well the Gaussian model fits the observed data and is given by

$$\chi^2_{red} = \frac{1}{n-p-1}\sum_{i=1}^{n}\frac{(f_i - y_i)^2}{\sigma^2}, \tag{3.6}$$

where n and p are the number of data points and the number of parameters being fitted, respectively, f_i is the theoretical function (3.4), y_i is the observed data, and

σ^2 is the variance in the observed data. Unfortunately, the variance is unknown for our case and is therefore said to equal one. χ^2_{red} is a one–dimensional function so, the method of steepest descent is modified some in that the partial derivative of χ^2_{red} will be taken with respect to each free parameter. An initial guess for A, x_0, σ, a and b is given. The partial derivative of χ^2_{red} is then taken with respect to each of the five parameters and evaluated at each data point from a given set of data points. The sum of the partial derivatives at each data point is taken for each parameter. Each sum is then multiplied by some small step size and the product is subtracted from the original value of the corresponding parameter. This procedure can be expressed as

$$p_{k,j+1} = p_{k,j} - d\left(\left.\frac{\partial \chi^2_{red}}{\partial p_k}\right|_j + \sum_{i=1}^{n} \left.\frac{\partial \chi^2_{red}}{\partial p_k}\right|_i\right), \tag{3.7}$$

where p_k is a specific parameter, d is the step size, $j+1$ indicates the new value of the k^{th} parameter, j indicates the old value of the k^{th} parameter and n is the number of data points. This new value for each parameter is substituted into the Gaussian function in the equation for χ^2_{red}. The result is compared to the previous value for χ^2_{red} which is initially some large number. Until the difference between the old χ^2_{red} and the new χ^2_{red} is $\leq 5 \times 10^{-8}$ for four consecutive iterations, the algorithm is repeated. The parameters which allow the conditions to be met are used to fit the Gaussian function to each peak.

To use the method of steepest descent, the five parameters need an initial guess. The initial guesses for the amplitude A, center x_0 and y–intercept b are found by fitting a fourth order polynomial to each of the six peaks from the radius–squared fringe profile. MATLAB 's polyfit function fits a polynomial of a specified order and outputs the coefficients of that polynomial. Figure 3.4 shows an example of one of

the peaks fitted with a fourth order polynomial using the polyfit function. To obtain the coordinates for the two minima and maximum the roots of the first derivative of the fitted polynomial is found. The center of the peak is determined by averaging the radius–squared index values of the two minima. This becomes the initial guess for x_0. Calculating the difference between the average intensity of the maximum and of one of the minimums provides an initial guess for the amplitude, A. From the first peak, the intensity value of the minimum located closest to the origin is used as the y–intercept. This b value is used when fitting each of the six peaks with the Gaussian function on one fringe pattern. Another feature extracted from the polynomial fit of each peak is the interval of data points which will be fitted with the Gaussian curve. This is found by determining the index of the two data points closest to the two minimums. Figure 3.4 shows and example of a peak fitted with a fourth order polynomial and its corresponding Gaussian fit.

The purpose of finding the initial guesses through the polyfit function is to essentially automate the routine of fitting each peak with a Gaussian function. Automating this process allows for the calculation of the horizontal winds to be as efficient as possible. The initial guesses for σ and a are hard–coded into the routine as 1 and 0, respectively.

The fitting procedure results in the identification of the center of each of the six transmission peaks of the radius–squared profile. This is necessary to calculate the horizontal winds. A value for the reduced chi square for every fit is also an output and will be used to calculate a weighted average of the individual winds. A value of $\chi^2_{red} = 1$ is said to indicate a good fit. A χ^2_{red} value greater than one indicates that the fit does not capture the data set well. On the other hand, a χ^2_{red} less than one suggests

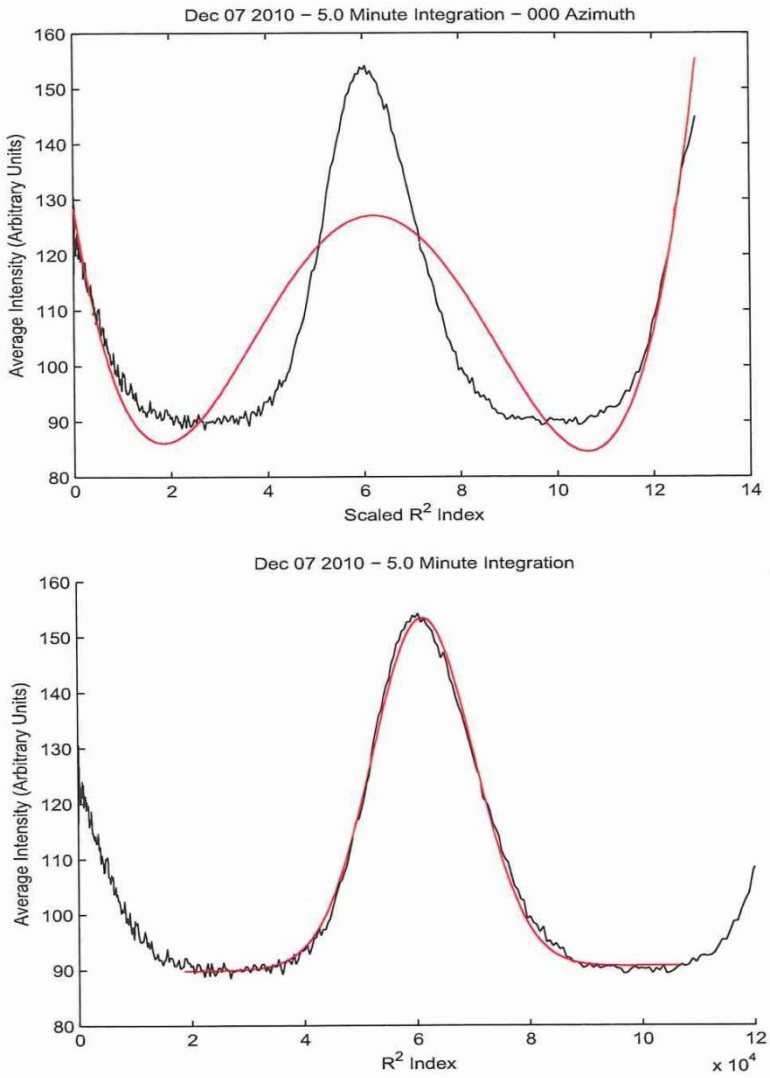

Figure 3.4: First peak fitted with a fourth order polynomial using MATLAB's polyfit function (left) and the corresponding Gaussian fit of the first peak (right) using the initial guesses obtained from the polynomial fit. The observed data is in black and the function that was fit to the peak is in red.

that the model is over–fitting the data. In general, if the number of parameters being fit is considerably less than the number of data points being fit, having a less than

one value for χ^2_{red} is another indication that the model is consistent with the observed data.

3.1.2 Calculating the Horizontal Winds

Six individual winds can be determined from a profile of two time–sequential, oppositely directed fringe patterns. In practice however, it was found that the sixth peak typically had a large χ^2_{red} value meaning the fit of the Gaussian curve was not consistent with the observed data points. As a result, the sixth peak was not used in the calculation of the average winds and therefore there was no need to fit the sixth peak. The remaining five peaks were fit with a Gaussian curve and the center in units of radius–squared CCD pixels of the Gaussian function corresponding to each peak is used to compute five individual winds. Figure 3.5 depicts five peaks of two radial profiles of opposite directions fitted with Gaussian curves.

From equation 3.3, the FSR of the zero–wind reference profile and the shift from the reference profile at a given order is required to calculate the LOS wind velocity. Using the determined peak centers, the zero–wind reference profile can be found. Consider Figure 3.5, the average of the two centers at each fringe order represents the centers of the peaks for the zero–wind reference profile. Finding the difference between the centers of two adjacent peaks leads to the zero–wind FSR. The zero–wind FSR can be calculated four times given the five peaks. For a given peak, the zero–wind FSR used to calculate the wind velocity is the FSR which was calculated using the center of the zero–wind profile peak at that order. The centers of the three interior peaks are used to calculate the zero–wind FSR to the right and left side of the peak therefore; the average of these two is used as the zero–wind FSR in radius–squared

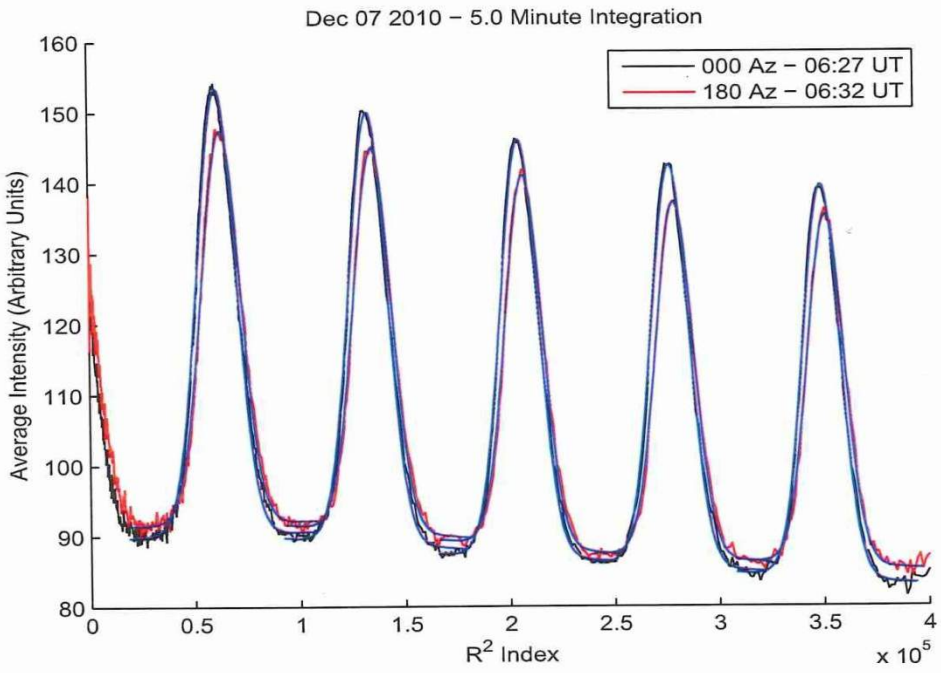

Figure 3.5: Two time–sequential fringe profiles of opposite directions where each peak is fit with a Gaussian curve (blue).

CCD pixels. The first and fifth peaks simply use the zero–wind FSR computed using the center of the zero–wind profile at those two corresponding orders. The shift from the reference profile at a particular order is found to be half the difference between the two centers of the directional profiles at that order. Finally, the resulting LOS wind velocity is then divided by the cosine of the viewing angle to obtain the horizontal wind. The viewing angle for the FPI at SPRL is 30 degrees.

The direction of the wind is determined by looking at which directional profile is shifted toward the origin. If the winds are toward the east for example, when the mirror is oriented to look west the winds will be traveling toward the mirror and the green line emission would appear to be blue–shifted, i.e., have a shorter wavelength. When the mirror faces east, the green line emission is red–shifted, appearing to have a longer wavelength. Looking at the equation $\lambda m = 2l\cos\theta$, at a particular order, a longer wavelength would correspond to a smaller angle. As a result, the longer wavelength would appear at a smaller radius on a fringe pattern [Guo]. On the radius–squared profile the position of the peaks created when the mirror is facing west will be to the right of the peaks produced from the mirror oriented toward the east. The sign convention follows that a wind toward the east and north is positive while a wind toward the west and south is negative.

3.1.3 Producing a Time Series

For two time–sequential, opposite direction radius–squared profiles, five individual winds are determined. A weighted average of the five individual winds is calculated so that there is one wind for a particular time. Before the weighted average is taken, however, the peaks which have a "bad" fit are filtered out. The average χ^2_{red} of each

order is compared to the average χ^2_{red} of the first peak. Because the Gaussian curve of the first peak is fitted to a greater number of points than the other peaks, the fit is thought to be more believable and therefore the wind from that order is more believable as well. If the average χ^2_{red} from the two peaks a specific order is greater than 25 percent of the average χ^2_{red} of the first peak, the wind corresponding to that order is not included in the weighted average. The following equation used to compute the weighted average uses the average χ^2_{red} value for each order

$$v_{avg} = \frac{\sum_{i=1}^{5} v_i \left(\frac{\chi_1^2}{\chi_i^2} \right)}{\sum_{i=1}^{5} \left(\frac{\chi_1^2}{\chi_i^2} \right)}. \tag{3.8}$$

Given the equation above, if the average χ^2_{red} value at a particular order is less than that of the first peak, the wind from that order is given more weight in the average. The converse holds true so, an order with an average χ^2_{red} value greater than that of the first peak will have less weight in the average.

The time associated with a particular wind is the midpoint of the time period in which the two opposite direction scans were taken. The time is given in Universal Time (UT) which is four hours ahead of Eastern Standard Time during daylight savings time and five hours ahead of Eastern Standard Time during the months of non-daylight savings time.

The error in the observed wind is found by taking the standard deviation between the five individual winds. The standard deviation, σ is

$$\sigma = \sqrt{\frac{\sum_{i=1}^{n} (x_i - \overline{x})^2}{n-1}}, \tag{3.9}$$

where n is the number of elements in the sample, $\overline{x}$ is the average of the sample and x_i is an individual element. The number of elements in the sample at most is five; there can be less if any peaks had been filtered out due to a "bad" fit. Error bars are seen in the time series of both wind components, meridional and zonal, as shown in the following chapter. The full length of an error bar is equal to two standard deviations. At a particular time, the average wind is given in meters per second with an error of plus or minus one standard deviation.

Chapter 4

Data Presentation & Discussion

4.1 Time Series Comparison with Model

Time series of the horizontal winds were produced for the months of November 2010, December 2010, January 2011, February 2011, March 2011, and April 2011. The time series for the last couple of days and/or the first couple of days of each month were compared with the Horizontal Wind Model (HWM07). The HWM07 is a statistical representation of the horizontal wind fields of the Earth's atmosphere from the ground to an altitude of 500 km [Drob et al., 2008]. It is the successor to the HWM93 of the Horizontal Wind Model series and represents observational data sets from satellite, rocket, and ground-based instruments from 1956 to 2007. Although stochastic variability from gravity waves and migrating planetary waves cannot be represented by the empirical model, migrating tides, non–migrating tides, and stationary planetary waves are able to be represented since monthly mean climatologies have been developed for those type of global–scale waves [Drob et al., 2008]. Since the wind profiles provided by the HWM07 does not change significantly day to day

the wind profile for Daytona Beach, FL (29° N, 81° W) for the first of every month was acquired. Observed data from the FPI at SPRL from the first of January, March, April, and December was compared to the HWM07. Figures 4.1, 4.2, 4.3, and 4.4 show this comparison for days around and on the first of those months.

For the winds observed around the first of January, the zonal component shows a west wind at the beginning of the night turning toward the east within the first couple of hours of the night. The eastward winds reach a maximum just before the middle of the night, around 5 UT. The meridional winds begin in the north for the most part and reach a maximum north wind around 4 UT before decreasing in magnitude and turning south for the last third of the night. Like the month of January, for the month of March the zonal component exhibits a wind to the west at the beginning of the night and turns easterly around 5 UT reaching a maximum just before twilight. The observed meridional wind is zero around nautical twilight and grows in magnitude to the south before turning north early in the night and reaching a maximum north wind around 5 UT and finally turning south before 10 UT. The southward wind in the beginning of the night is uncharacteristic of the model, it is however seen in the observed winds around the beginning of the month in April as well. April's meridional winds demonstrate a maximum north wind before 10 UT and then decreases in magnitude but does not turn south like the model depicts. For the observed zonal component at the beginning of April, the winds are primarily north. There is a southward wind for one to three hours during the first half of the night. The beginning of the month of December however, seems to be out of phase with the model specifically the zonal component. Both components of the observed winds of November 30th especially looks like the negative of the model. The meridional winds

observed on December 1st and 2nd show a maximum around 5 UT which is similar to the model. On the other hand, the zonal winds of both days seems to be out of phase with the model. Overall, the depicted observed winds follow the general trend of the HWM07 with the exception of the observed winds around the beginning of December.

The average of the observed meridional and zonal winds from mid–December to mid–January was calculated and compared with the wind profile given by the HWM07 for the first of January (Figure 4.5). The average meridional winds seems to be consistent with the model unlike the average zonal winds which tends to increase in magnitude to the east instead of decreasing during the second half of the night. The average of the observed winds from mid–November to mid–December was also compared with the HWM07 wind profile for the first of December (Figure 4.6). Although the average winds are consistent with the observed winds depicted for the beginning of December (Figure 4.4) the average seems to be out of phase with the wind profile given by the model. Though not in phase with the HWM07, the average winds are of the same magnitude as the model.

The scope of this thesis was not only to produce horizontal winds from the FPI at SPRL but to also identify atmospheric gravity waves from them. The following section will discuss this part.

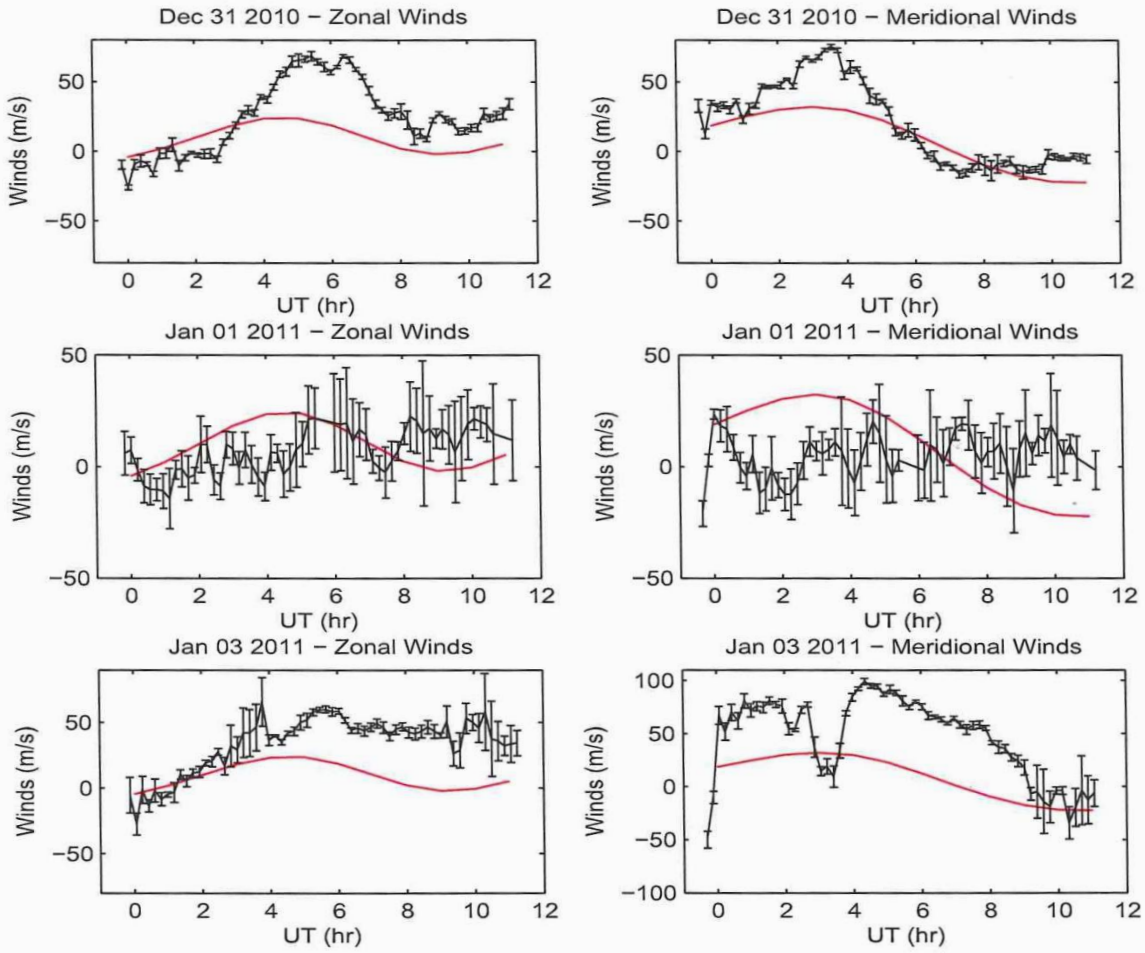

Figure 4.1: Comparison of observed horizontal winds (black) at Daytona Beach for the nights of December 31st, January 1st, and January 3rd with the HWM07 (red). The wind profile produced by the HWM07 represents the winds for the night of January 1st. Positive winds are north and east for the meridional and zonal winds, respectively.

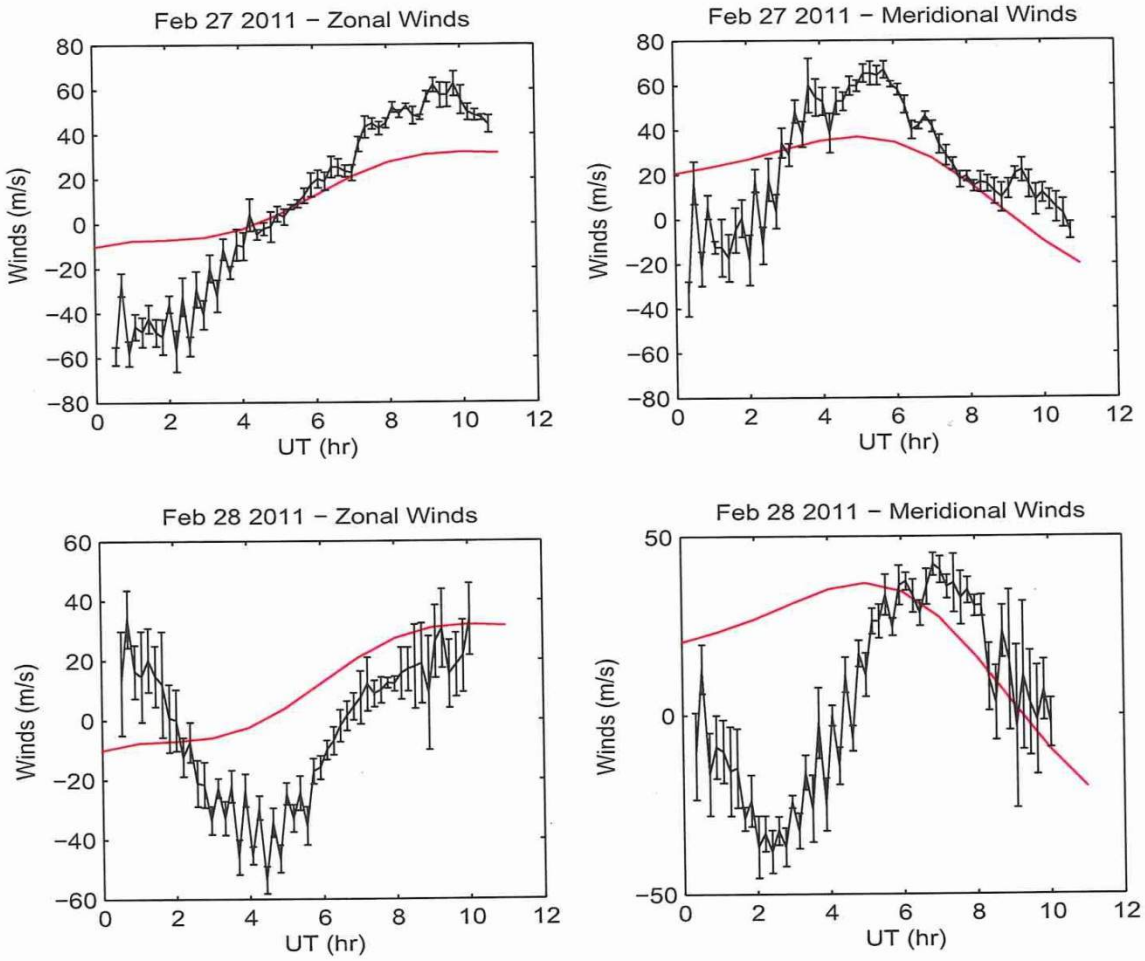

Figure 4.2: Comparison of observed horizontal winds (black) at Daytona Beach for the nights of February 27th and February 28th with the HWM07 (red). The wind profile produced by the HWM07 represents the winds for the night of March 1st. Positive winds are north and east for the meridional and zonal winds, respectively.

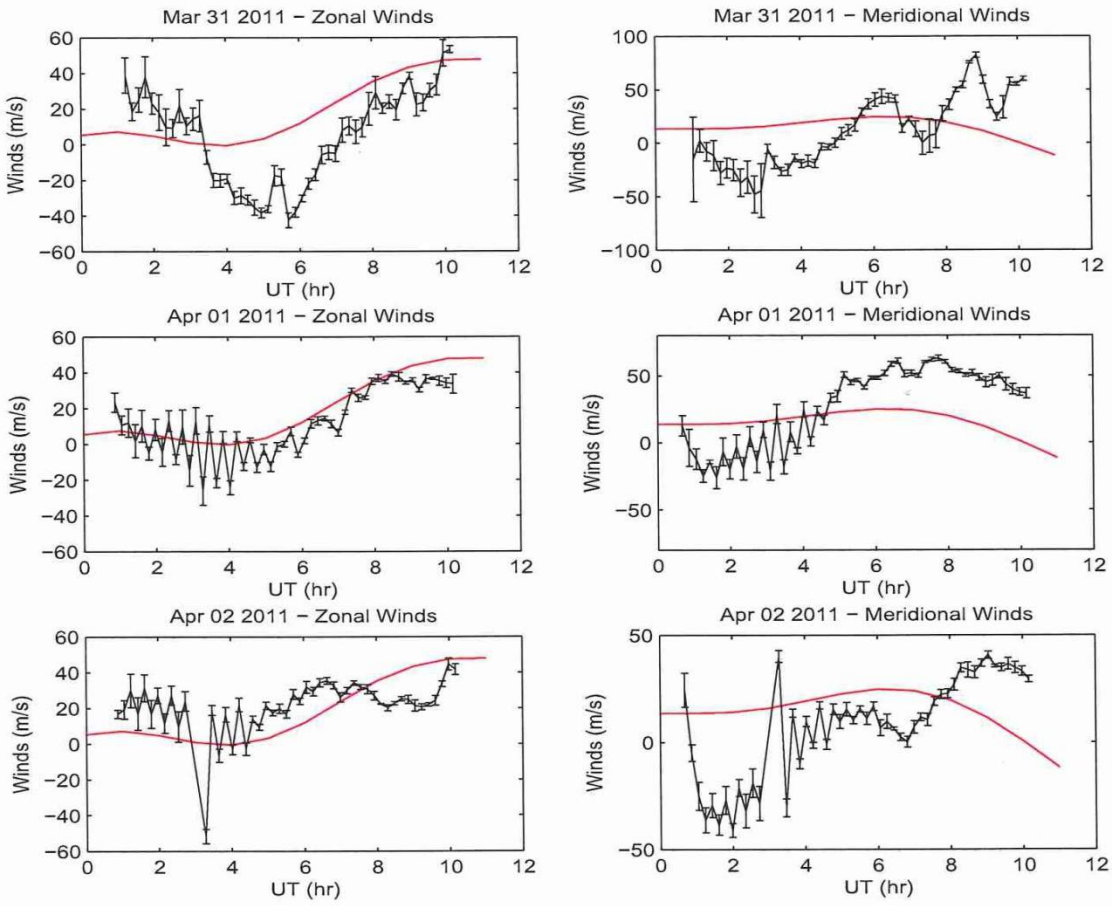

Figure 4.3: Comparison of observed horizontal winds (black) at Daytona Beach for the nights of March 31st, April 1st, and April 2nd with the HWM07 (red). The wind profile produced by the HWM07 represents the winds for the night of April 1st. Positive winds are north and east for the meridional and zonal winds, respectively.

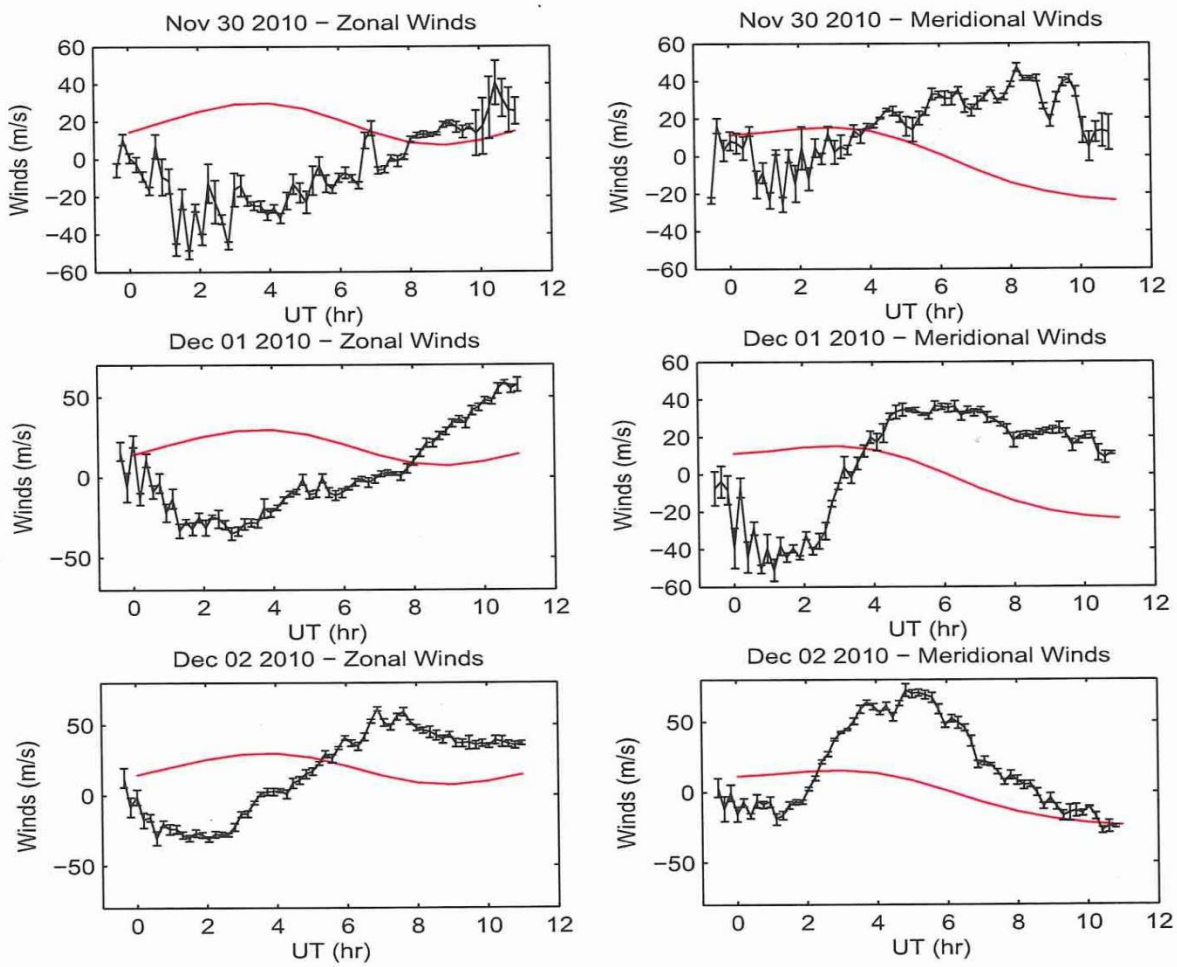

Figure 4.4: Comparison of observed horizontal winds (black) at Daytona Beach for the nights of November 30th, December 1st, and December 2nd with the HWM07 (red). The wind profile produced by the HWM07 represents the winds for the night of December 1st. Positive winds are north and east for the meridional and zonal winds, respectively.

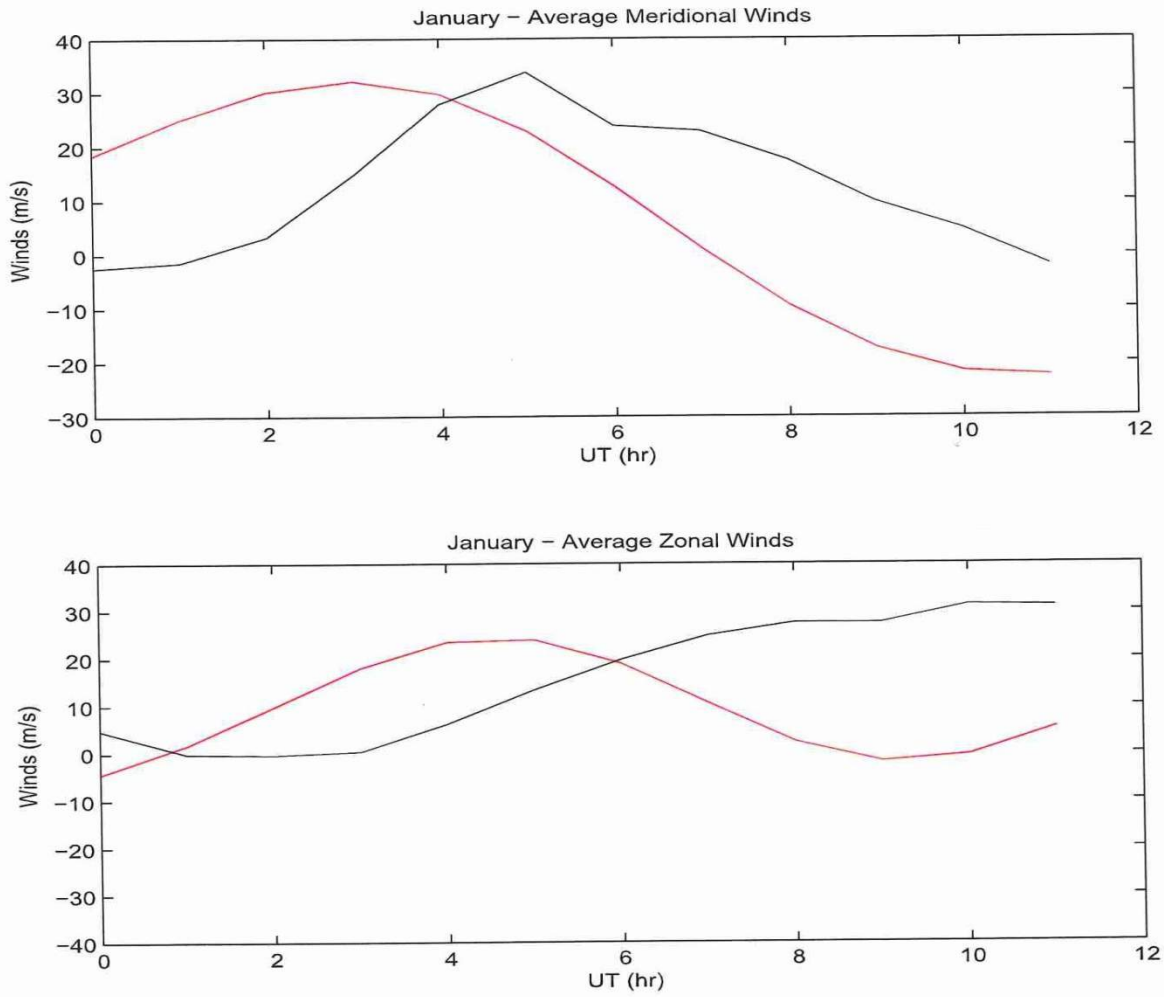

Figure 4.5: Average meridional (top) and zonal (bottom) winds for the month of January. The winds observed from the SPRL FPI (black) are compared with the wind profile given by the HWM07 (red) for the night of January 1st. Positive winds are north and east for the meridional and zonal winds, respectively.

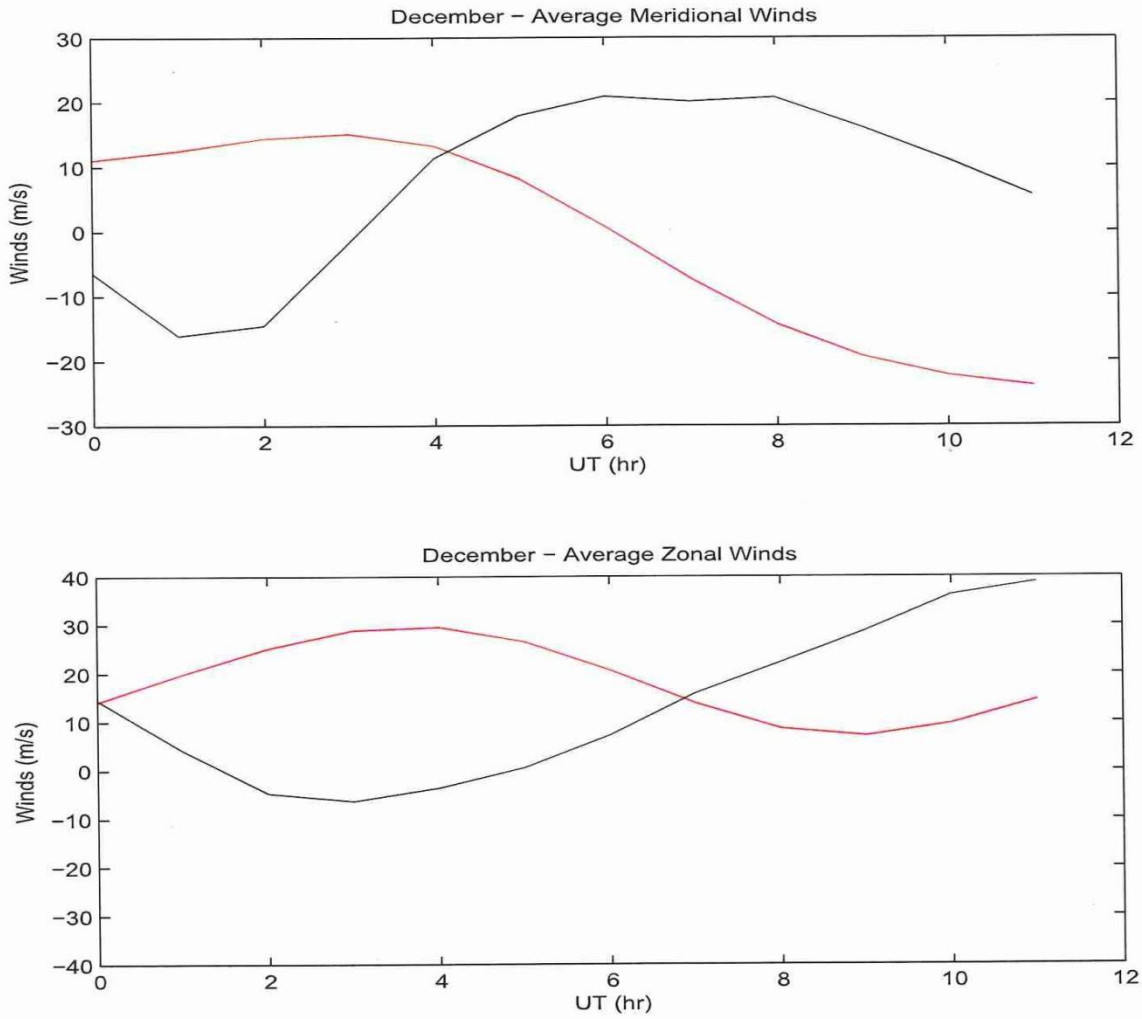

Figure 4.6: Average meridional (top) and zonal (bottom) winds for the month of December. The winds observed from the SPRL FPI (black) are compared with the wind profile given by the HWM07 (red) for the night of December 1st. Positive winds are north and east for the meridional and zonal winds, respectively.

4.2 Power Spectra

In order to identify intrinsic oscillations within the horizontal wind time series, specifically those of atmospheric gravity waves, Fourier analysis was performed on the time series. A Fast Fourier Transform (FFT) was executed to transform the time series from the time domain to the frequency domain . The FFT function in MATLAB was used to create a power spectrum from the winds. A sliding FFT was employed to create a dynamic power spectrum which allows one to see the progression of oscillations with time. The window which was chosen for the sliding FFT was three hours and was slid one hour. Both the static and dynamic spectra were normalized with respect to the global maximum power.

Fourier analysis on the time series from three different days will be presented and discussed. The weather to the west of Daytona Beach differs each night; one night had clear conditions, one night there was a thunderstorm to the west, one night there were some rain showers on the west coast of Florida . The corresponding power spectrum of each night depicts the different meteorological behavior.

4.2.1 Case 1: Clear Weather

The night of December 2, 2010 was clear across the entire state of Florida as well as off the east and west coast. The peak in the spectra of both the meridional and zonal component seen in Figure 4.7 corresponds to the shorter period modes of the diurnal tide. Since the time series is at most 11.55 hours long, the semi–diurnal tide with a period of 12 hours as well as the diurnal tide with a period of 24 hours would not be included in this peak therefore, the smaller harmonics of the diurnal tide is represented. The bin of this peak centered at the frequency 0.0872 hr^{-1} contains

periodicities with periods between 22.94 hr and 7.65 hr. The frequency with the second highest power is 0.1744 hr^{-1} and contains oscillations with periods between 7.65 hr and 4.59 hr. Again, shorter period tidal modes would be included within this bin. A small amount of power is seen in the following two frequencies in the spectral power of the zonal winds. The bins of the two frequencies together include periods between 4.59 hours and 2.55 hours. There is very little to no power at higher frequencies.

4.2.2 Case 2: Cloudy and Rainy Weather

During the night of December 17, 2010 there were clouds and rain showers along the west coast of Florida. This weather activity can be seen in the power spectra of December 17th. In addition to the strong tidal oscillations, weaker high frequency waves are present as well. The power spectra of both the meridional and zonal components (Figure 4.8) show the smaller harmonics of the diurnal tide like the night of December 2nd. Because there is a short time separation between days, December 17th and December 2nd, the length of the two time series is the same. Therefore, the frequency at which the peak in the power spectra for December 17th is 0.0872 hr^{-1} and the corresponding frequency bin contains periods between 22.94 hr and 7.65 hr. Also, the locations of the tidal features in the dynamic power spectra are similar in the dynamic power spectra of December 2nd and December 17th. The shorter period tidal modes are also present in both components' spectral power like in the spectral power diagram for December 2nd. Between the frequencies of 1 hr^{-1} and 2 hr^{-1} there are a couple of frequencies which exhibit some power toward the end of the night. A greater amount of power is seen in frequencies greater than 2 hr^{-1} which correspond

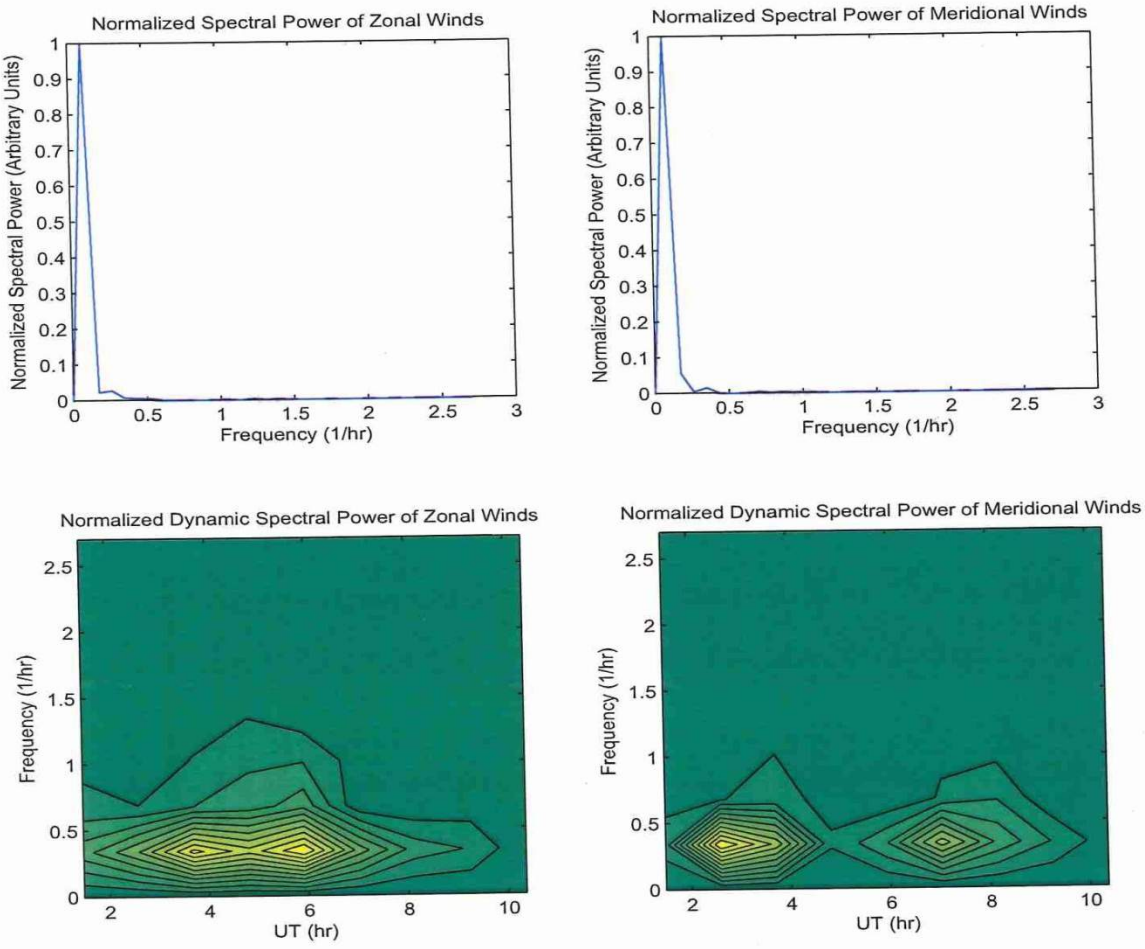

Figure 4.7: Case 1: Normalized spectral power and normalized dynamic spectral power for the zonal and meridional winds from the night of December 2, 2010. The yellow color in the normalized dynamic spectral power indicates strong power while the darker the green the weaker the power.

to oscillations with periods on the order of 20 or 30 minutes. These are seen in the dynamic spectral power, specifically of the meridional winds, in the upper left corner (see Figure 4.8).

4.2.3 Case 3: Thunderstorm

A thunderstorm off the west coast of Florida during the night of March 27, 2011 was apparent in the results of the spectral power of both wind components for that night. Figure 4.9 displays the normalized spectral power and normalized dynamic spectral power for the meridional and zonal wind components. The first strong peak as seen in the other power spectra correspond to the smaller tidal mode of 8 hr. For this time series however, the peak is centered at a frequency of 0.104 hr^{-1} because the time series length is shorter than the previously discussed days in December. The frequency bin for this peak includes frequencies from 0.0519 hr^{-1} to 0.156 hr^{-1} which correspond to periods of 19.24 hr and 6.41 hr. Shorter period tidal modes are present as well.

Note the peak with an observed frequency of 1.663 hr^{-1} in the spectral power of the zonal winds. The peak most likely represents an atmospheric gravity wave produced by the thunderstorm on the west coast. The wave's peak frequency corresponds to a wave period of 36 min. This feature is seen in the spectral power of the meridional winds but at a peak frequency of 1.559 hr^{-1}, or period of 38.5 min. The strong tidal features in the meridional spectrum most likely shifted the gravity wave's peak observed frequency [Correspondence with Dr. Alan Liu].

Accordingly, the direction of propagation of the atmospheric gravity wave identified with respect to the background wind can be determined. Using the polarization

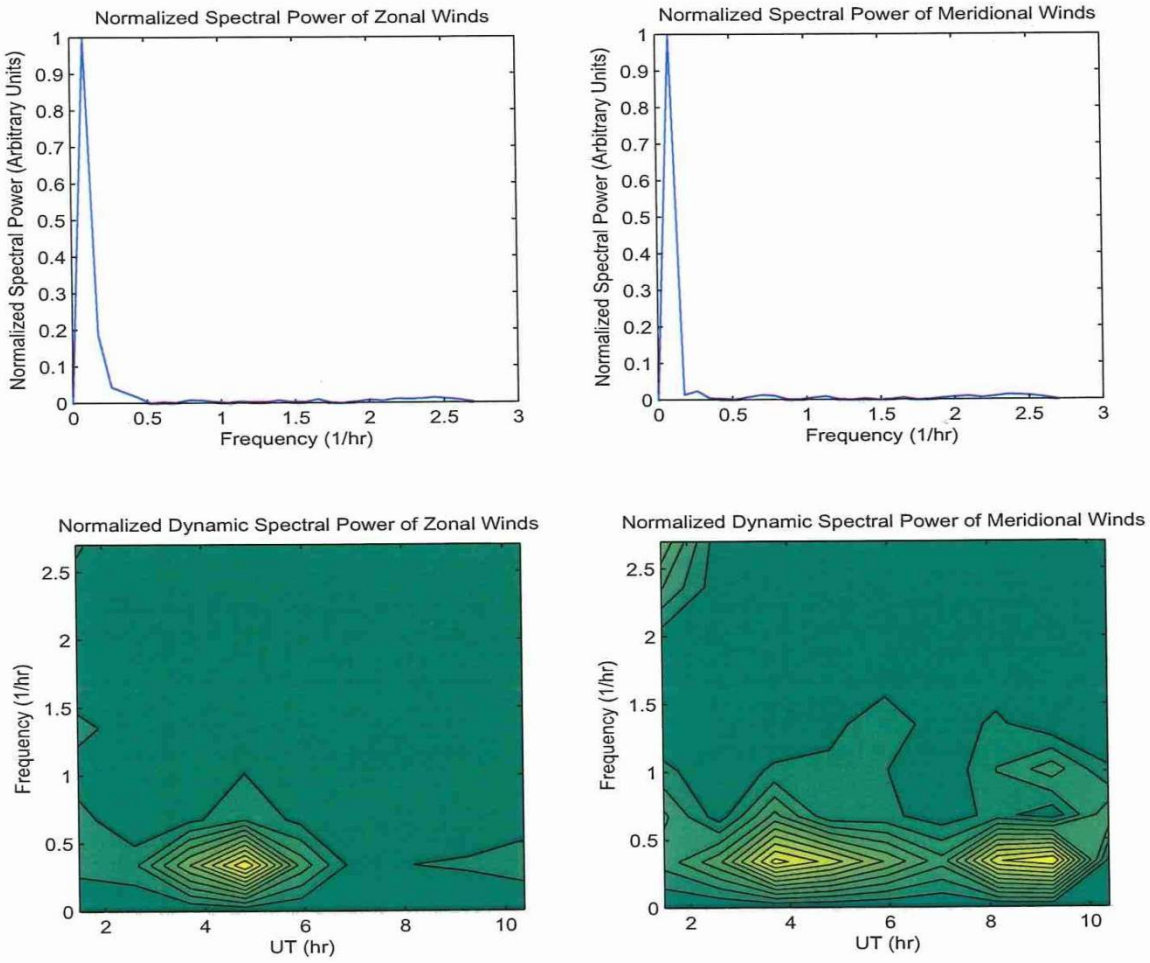

Figure 4.8: Case 2: Normalized spectral power and normalized dynamic spectral power for the zonal and meridional winds from the night of December 17, 2010. The yellow color in the normalized dynamic spectral power indicates strong power while the darker the green the weaker the power.

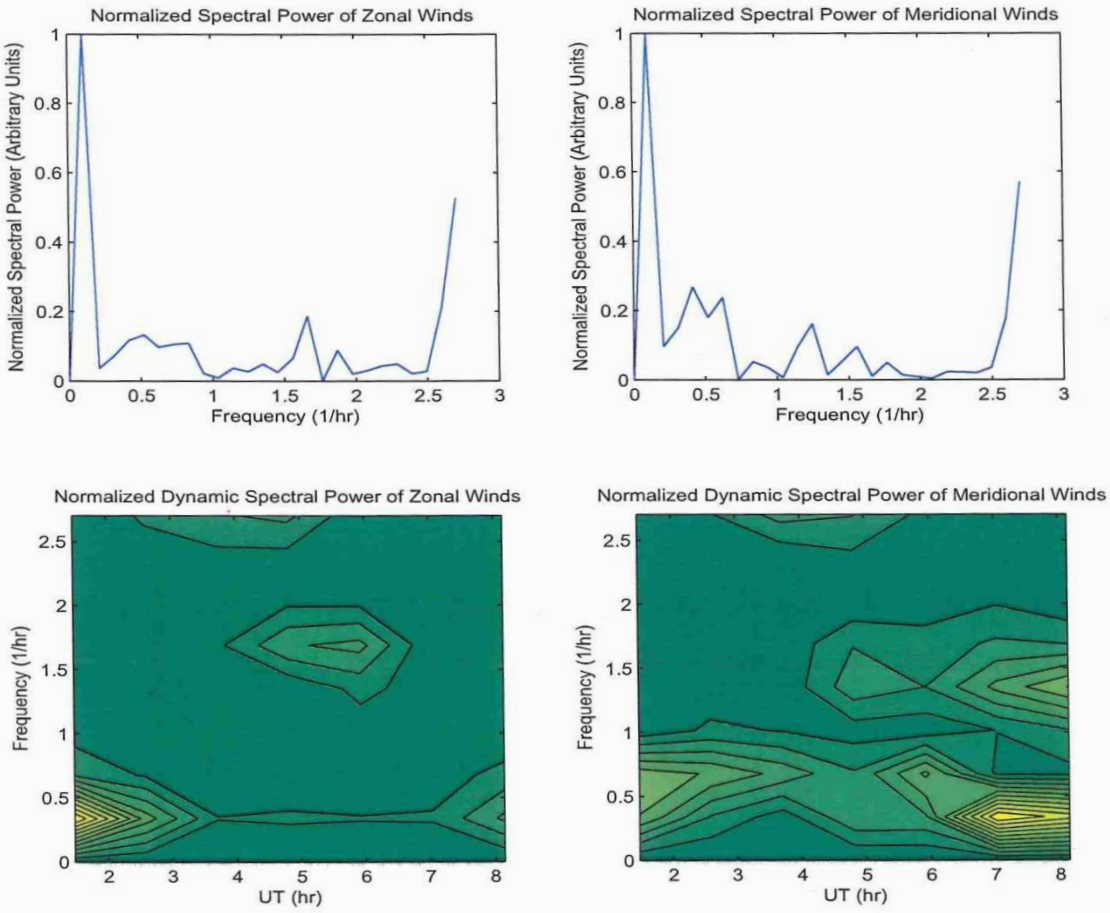

Figure 4.9: Case 3: Normalized spectral power and normalized dynamic spectral power for the zonal and meridional winds from the night of March 27, 2011. The yellow color in the normalized dynamic spectral power indicates strong power while the darker the green the weaker the power.

relations for gravity waves, the intrinsic wave frequency and propagation direction is found. From Hines' [1960] description of atmospheric gravity waves, the polarization relations are as follows

$$\tilde{u} = gH\frac{\omega k + ilf}{\omega^2 - f^2}\tilde{p} \tag{4.1}$$

and

$$\tilde{v} = gH\frac{\omega l - ikf}{\omega^2 - f^2}\tilde{p}, \tag{4.2}$$

where g is the acceleration due to gravity, H is the scale height, f is the Coriolis parameter, $\tilde{u}$, $\tilde{v}$, and $\tilde{p}$ are the complex amplitudes in the plane wave representations of the zonal and meridional wind and pressure perturbations in the form

$$u' = Re[\tilde{u}e^{i(kx+ly+mz-wt)}], \tag{4.3}$$

k, l, and m are the wave numbers in the x, y, and z–directions, respectively, and ω is the angular frequency of the wave. The phase difference between the zonal and meridional components is

$$\frac{\tilde{u}}{\tilde{v}} = \frac{\omega k + ilf}{\omega l - ikf} = Ae^{i\phi}, \tag{4.4}$$

where ϕ is the phase difference and A is the amplitude ratio of u' to v' [Correspondence with Dr. Alan Liu]. The phase difference and amplitude can then be written as

$$\tan\phi = \frac{1 + (l/k)^2}{(\omega/f - f/\omega)(l/k)} \tag{4.5}$$

$$A = \sqrt{\frac{1 + (l/k)^2(f/\omega)^2}{(l/k)^2 + (f/\omega)^2}}. \tag{4.6}$$

The quantity (l/k) is used to determine the direction of propagation [Correspondence with Dr. Liu]. However, the wave frequency is unknown in the two equations above. The amplitude and phase is given through the Fourier transform of both the meridional and zonal winds thus the amplitude ratio and phase difference is known. Therefore, equations 4.5 and 4.6 can be solved numerically to find (l/k) and ω.

Newtons method for a system of nonlinear equations was used to solve equations 4.5 and 4.6 for both the meridional and zonal winds . Notice that the system of equations will give two solutions for (l/k) and ω. The two calculated intrinsic frequencies of the gravity wave depicted in the power spectrum of the zonal component are 0.0622 hr^{-1} and -0.0622 hr^{-1}. Given that one solution results in a negative intrinsic frequency, that solution is rejected and the accepted solution is the one that gives an intrinsic frequency of 0.0622 hr^{-1}. The corresponding direction of propagation of the wave is the inverse tangent of the calculated quantity (l/k) which is 330.7° counter–clockwise from east. Figure 4.10 shows the dynamic spectral power with arrows representing the propagation direction of the oscillations with higher power. The two solutions are shown for both the meridional and zonal components.

The accepted solution can also be verified by knowing the direction of the wind at the time of the wave peak. Since the intrinsic wave frequency (0.0622 hr^{-1}) is smaller than the observed wave frequency (1.663 hr^{-1}), the wave is being Doppler shifted to a higher frequency therefore, it is propagating with the background wind [Nappo, 2002]. The direction of the arrow from the gravity wave should then match the direction of the observed wind around the time of the wave peak. From Figure 4.11 it can be seen that around 6 UT the zonal winds are toward the east and the meridional winds are toward the south for the most part. The observed wind direction therefore agrees

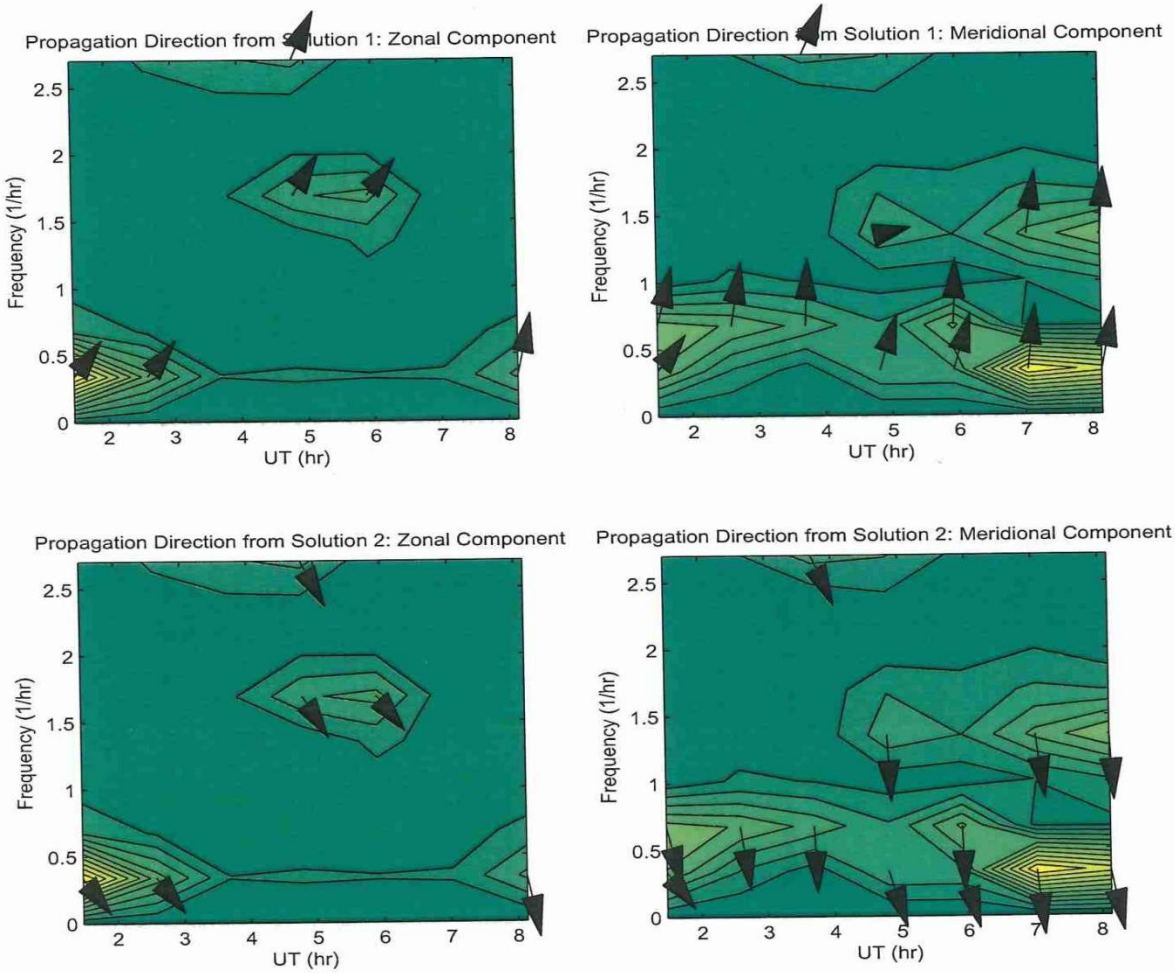

Figure 4.10: Direction of propagation of the higher power oscillations in the zonal and meridional winds for the night of March 27th represented by the black arrows. The soulution 1 is the rejected solution and solution 2 is the accepted solution. The orientation of the direction follows the cardinal directions, i.e. to the right is east, north is pointed to the top of the page.

with the southeast direction of the arrow representing the propagation direction of the gravity wave identified.

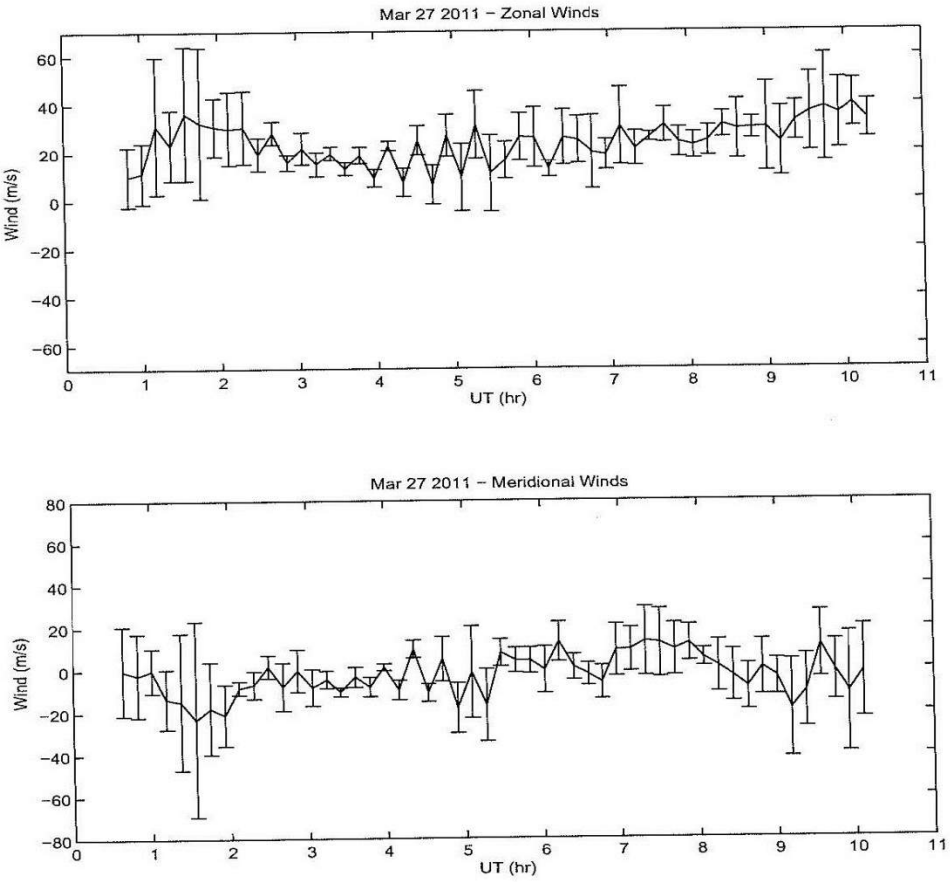

Figure 4.11: Observed zonal and meridional winds during the night of March 27, 2011 at Daytona Beach, FL.

Chapter 5

Concluding Remarks

5.1 Summary

The mesopause region is the least understood region of Earth's atmosphere. Characterized as the altitude range in which turbulent mixing transitions to molecular diffusion, the dynamics of the upper mesosphere and lower thermosphere are both complex and variable. Atmospheric gravity waves have been recognized as a major source of momentum and energy into the mesosphere and lower thermosphere as well as a major factor in the dynamic coupling between the troposphere and lower thermosphere. Due to there purely random nature and various sources they have been of significant interest since they were first suggested by Hines in 1960 and widely studied.

An atmospheric gravity wave produced by a thunderstorm has been identified through the analysis of the horizontal neutral winds observed by the Fabry–Perot interferometer at Embry–Riddle Aeronautical University's Daytona Beach, FL campus. The observed frequency of the wave was 1.663 hr^{-1} and the calculated intrinsic

frequency was 0.062 hr^{-1}. The determined direction of propagation of the wave was in agreement with the direction of the background winds for the night of March 27, 2011. Not only was a gravity wave identified but it was observed that there was a correlation between weather activity and the appearance of higher frequency oscillations in the spectral analysis of the wind time series.

In addition to the results from the spectral analysis of the winds, it was shown that the observed wind time series from the FPI at Embry-Riddle and the wind profiles produced by the HWM07 for Daytona Beach, FL exhibited similar trends for the nights around the beginning of the months of January, March and April of 2011. The month of December 2010 was the anomaly as the depicted wind time series seemed to be out of phase with the HWM07. This oddity would be interesting to consider in more detail in the future.

5.2 Future Work

The procedure developed in this thesis to output wind time series of horizontal neutral winds through the detection of Doppler shifts in the atomic oxygen nightglow can be used in many ways in the future. Placement with a second ground–based instrument to compare wind measurements is a possibility which could later improve long–term horizontal wind models. Simultaneous temperature measurements from another instrument have been used in the past to determine the coupling between winds and temperature and could be researched more in the future as well. Finally, the Fabry–Perot interferometer at SPRL has the ability to detect shifts in the atomic oxygen red line, another nightglow emission line which originates from an altitude of 250 km and has a wavelength of 6300 Å . Observations of winds from this region

would be advantageous as it would help characterize the upper atmosphere.

Other future work includes improvements that could be made to the work presented in this thesis. Wavelet analysis could be used as a second method of studying the spectral power of the winds instead of solely the Fourier transform method. Also, the configuration of the Fabry–Perot interferometer at SPRL could be altered by replacing the scanning mirror with a fish eye lens thus producing an imaging Fabry–Perot interferometer. Imaging Fabry–Perot interferometers have been successfully employed to measure horizontal winds of the upper atmosphere. This type of instrument can achieve better time resolution in the wind time series since all looking directions are imaged in one scan. The technique used to extract the horizontal winds would then need to be modified. The ultimate goal for the work presented and future work is to better characterize and understand the mesosphere/lower thermosphere region of Earth's atmosphere.

References

Fabry–perot interferometer. `http://www.scientific-web.com/en/Physics/Optics/FabryPerotInterferometer.html`. [Figure].

Image archive meterological case study selection kit, 2007. `http://locust.mmm.ucar.edu/`.

Nambath K. Balachandran. Gravity waves from thunderstorms. *Monthly Weather Review*, 108:804–816, 1980.

Manfred A. Biondi, Dwight P. Sipler, Mark E. Zipf, and Jeffrey L. Baumgardener. All-sky doppler interferometer for thermospheric dynamics studies. *Applied Optics*, 34:1,646–1,654, 1995.

R. Chattopadhyay and S.K. Midya. Airglow emissions: fundamentals of theory and experiment. *Indian Journal of Physics*, 80:115–166, 2006.

Thomas E. Cravens. *Physics of Solar System Plasmas.* Cambridge University Press, Cambridge, United Kingdom, 1997.

M.J. Curry and R.C. Murty. Thunderstorm-generated gravity waves. *Journal of Atmospheric Sciences*, 31:1402–1408, 1974.

D.P. Drob, J.T. Emmert, G. Crowley, J.M. Picone, G.G. Shepherd, W. Sinner, P. Hays, R.J. Niciejewski, M. Larsen, C.Y. She, J.W. Meriwether, G. Hernandez, M.J. Jarvis, D.P. Sipler, C.A. Tepley, O'Brien M.S., J.R. Bowman, Q. Wu, Y. Murayama, S. Kawamura, I.M. Reid, and R.A. Vincent. An empirical model of the earth's horizontal wind fields: Hwm07. *Journal of Geophysical Research*, 113, 2008.

NASA Space Physics Data Facility. MSIS–E–90 Atmosphere Model. `http://omniweb.gsfc.nasa.gov/vitmo/msis_vitmo.html`.

David C. Fritts. Gravity wave forcing and effects in the mesosphere and lower thermosphere. In *The Upper Mesosphere and Lower Thermosphere: A Review of Experiment and Theory*, pages 89–98. American Geophysical Union, 1995a.

David C. Fritts. Tidal and planetary waves. In *The Upper Mesosphere and Lower Thermosphere: A Review of Experiment and Theory*, pages 67–87. American Geophysical Union, 1995b.

T.J. Fuller-Rowell. The dynamics of the lower thermosphere. In *The Upper Mesosphere and Lower Thermosphere: A Review of Experiment and Theory*, pages 23–36. American Geophysical Union, 1995.

D. Gobbi, H. Takahashi, B.R. Clemesha, and P.P. Batista. Equatorial atomic oxygen profiles derived from rocket observations of oi 557.7 nm airglow emission. *Planetary and Space Science*, 40:775–781, 1992.

E.M. Griffin, A.L. Aruliah, I. McWhirter, H.-C.I. Yiu, A. Charalambous, and I. McCrea. Upper thermospheric wind and temperature measurements from an extended spatial field. *Annales Geophysicae*, 26:2649–2655, 2008.

Atmospheric Emissions Group. `http://sprg.ssl.berkeley.edu/atmos/gj_science.html`. [Figure].

Weiji Guo. *F-region Winds Over the Central Polar Cap.* PhD thesis, University of Saskatchewan.

Anthony R. Hansen, Gregory D. Nastrom, Jason A. Otkin, and Frank D. Eaton. Mst radar observations of gravity waves and turbulence near thunderstorms. *Journal of Applied Meteorology*, 41:298–304, 2002.

G. Hernandez. *Fabry-Perot Interferometers.* Cambridge University Press, Cambridge, United Kingdom, 1986.

C.O. Hines. Internal atmospheric gravity waves at ionospheric heights. In *The Upper Atmosphere in Motion, A Selection of Papers With Annotation*, pages 247–328. American Geophysical Union, 1960.

C.O. Hines. The upper atmosphere in motion. In *The Upper Atmosphere in Motion, A Selection of Papers With Annotation*, pages 13–93. American Geophysical Union, 1962.

John M. Hughes. The earth's neutral atmosphere. EP 410 Lecture PPT, 2008.

John M. Hughes. fabry_perot_fringe_center.m, 2009.

John M. Hughes. Observations of midlatitude neutral winds using a high throughput fabry–perot interferometer. Florida Space Grant Proposal, 2010.

M. Ishii, S. Oyama, R. Fuji, E. Sagawa, S. Watari, and H. Shinagawa. Dynamics of neutral wind in the polar region observed with two fabry-perot interferometers. *Earth Planets Space*, 51:833–844, 1999.

Mamoru Ishii, Shoichi Okano, Eiichi Sagawa, Shin'ichi Watari, Hirotaka Mori, Iwao Iwamoto, and Yasuhiro Murayama. Development of fabry-perot interferometers for airglow observations. In *Proceedings of the NIPR Symposium on Upper Atmosphere Physics*, volume 10, pages 97–108, 1997.

Erik Johnson. arrow.m, 2009. MATLAB function to produce arrows.

A. Raymond Jordan. Atmospheric gravity waves from winds and storms. *Journal of the Atmospheric Sciences*, 29:445–456, 1972.

Stella M.L. Melo, Hisao Takahashi, B.R. Clemesha, P. Batista, and D.M. Simonich. Atomic oxygen concentration from rocket airglow observations in the equatorial region. *Journal of Atmospheric and Terrestrial Physics*, 58:1,935–1,942, 1996.

J.W. Meriwether, M.A. Biondi, F.A. Herrero, C.G. Fesen, and D.C. Hallenback. Optical interferometric studies of the nighttime equatorial thermosphere: Enhanced temperatures and zonal wind gradients. *Journal of Geophysical Research (or J. Geophys. Res.)*, 102:20,041–20,058, 1997.

Carmen J. Nappo. *An Introduction to Atmospheric Gravity Waves*. Academic Press, San Diego, California, 2002.

Frank L. Pedrotti, Leno S. Pedrotti, and Leno M. Pedrotti. *Introduction to Optics.* Pearson Prentice Hall, New Jersey, 3rd edition edition, 2007.

William H. Press, Saul A. Teukolsky, William T. Vetterling, and Brian P. Flannery. *Numerical Recipes in C: The Art of Scientific Computing.* Cambridge University Press, Cambridge, United Kingdom, 2nd edition edition, 1992.

Gerd W. Prolss. *Physics of the Earth's Space Environment.* Springer, Germany, 2004.

M.H. Rees. *Physics and Chemistry of the Upper Atmosphere.* Cambridge University Press, Great Britain, 1989.

F.E. Roach. Diurnal and seasonal variation of the airglow. *Proceedings of the National Academy of Sciences of the U.S.A.*, 40:950–956, 1954.

Raymond G. Roble. Energetics of the mesosphere and thermosphere. In *The Upper Mesosphere and Lower Thermosphere: A Review of Experiment and Theory*, pages 1–21. American Geophysical Union, 1995.

K. Shiokawa, T. Kadota, Y. Otsuka, T. Ogawa, T. Nakamura, and S. Fukao. A two-channel fabry-perot interferometer with thermoelectric-cooled ccd detectors for neutral wind measurement in the upper atmosphere. *Earth Planets Space*, 55: 271–275, 2003.

M.J. Taylor, V. Taylor, and R. Edwards. An investigation of thunderstorms as a source of short period mesospheric gravity waves. In *The Upper Mesosphere and Lower Thermosphere: A Review of Experiment and Theory*, pages 177–184. American Geophysical Union, 1995.

Alan C. Tribble. *The Space Environment: Implications for Spacecraft Design.* Princeton University Press, Princeton, New Jersey, 2003.

P. Vila, D. Rees, P. Merrien, and E. Kone. Fabry-perot interferometer measurements of neutral winds and f2 layer variations at the magnetic equator. *Annales Geophysicae (or Ann. Geophys)*, 16:731–737, 1998.

Won Young Yang, Wenwu Cao, Tae-Sang Chung, and John Morris. *Applied Numerical Methods Using MATLAB.* John Wiley & Sons, Inc., New Jersey, 2005.